

OPTIMIZATION OF LASER PROCESSING FOR PERC TYPE C-SI SOLAR
CELLS

A THESIS SUBMITTED TO
THE GRADUATE SCHOOL OF NATURAL AND APPLIED SCIENCES
OF
MIDDLE EAST TECHNICAL UNIVERSITY

BY

EZGİ GENÇ

IN PARTIAL FULFILLMENT OF THE REQUIREMENTS
FOR
THE DEGREE OF MASTER OF SCIENCE
IN
MICRO AND NANOTECHNOLOGY

AUGUST 2019

Approval of the thesis:

OPTIMIZATION OF LASER PROCESSING FOR PERC TYPE C-SI SOLAR CELLS

submitted by **EZGİ GENÇ** in partial fulfillment of the requirements for the degree of **Master of Science in Micro and Nanotechnology Department, Middle East Technical University** by,

Prof. Dr. Halil Kalıpçılar
Dean, Graduate School of **Natural and Applied Sciences**

Prof. Dr. Almıla Güvenç Yazıcıoğlu
Head of Department, **Micro and Nanotechnology**

Prof. Dr. Raşit Turan
Supervisor, **Micro and Nanotechnology, METU**

Assoc. Prof. Dr. Görkem Günbaş
Co-Supervisor, **Chemistry, METU**

Examining Committee Members:

Assoc. Prof. Dr. Alpan Bek
Physics, METU

Prof. Dr. Raşit Turan
Micro and Nanotechnology, METU

Assist. Prof. Dr. Ihor Pavlov
Physics, METU

Assist. Prof. Dr. Selçuk Yerci
Micro and Nanotechnology, METU

Assist. Prof. Dr. Veysel Ünsür
Energy Systems Eng., Necmettin Erbakan Uni.

Date: 20.08.2019

I hereby declare that all information in this document has been obtained and presented in accordance with academic rules and ethical conduct. I also declare that, as required by these rules and conduct, I have fully cited and referenced all material and results that are not original to this work.

Name, Surname: EZGİ GENÇ

Signature:

ABSTRACT

OPTIMIZATION OF LASER PROCESSING FOR PERC TYPE C-SI SOLAR CELLS

GENÇ, EZGİ

Master of Science, Micro and Nanotechnology

Supervisor: Prof. Dr. Raşit Turan

Co-Supervisor: Assoc. Prof. Dr. Görkem Günbaş

August 2019, 75 pages

Passivated Emitter Rear Contact (PERC) type solar cells, which currently owns a similar market share as the standard type solar cells, is expected to be the dominant type of the photovoltaic (PV) market in near future (ITRPV, 2019) due to its high performance/cost ratio. Hence, it is critical to optimize PERC process steps to achieve higher efficiencies. In PERC concept, the stack of a passivation layer and SiN_x capping layer is locally ablated to form low recombination and low resistive contacts. In this way, the total recombination at the rear side of the wafer is significantly reduced, leading to a higher open-circuit voltage and charge collection efficiencies in the base of the cell. In this thesis, the experiments which mainly focus on rear local contact formation were conducted with a picosecond laser of 532 nm wavelength to create local contact openings (LCOs). To determine the best laser performance in LCO process, the contact characteristics such as Al:BSF depth, contact width after firing, void fraction were correlated to laser fluence. To see the effects of these contact characteristics on solar cell performance and determine an optimized fluence range, efficiencies of the solar cells that were produced for each fluence were compared. For more detail investigation, corresponding efficiencies were calculated using Quokka simulation. Subsequently, the laser ablation process was optimized for the PERC

production in Günam Photovoltaic Line (GPVL) and %19 efficiency has been achieved for the industrial-scale.

Keywords: PERC type c-Si solar cells, Laser ablation process, Rear contact formation, Rear contact characteristics

ÖZ

PERC TİPİ C-Sİ GÜNEŞ HÜCRELERİ İÇİN LAZER PROSESİ OPTİMİZASYONU

GENÇ, EZGİ

Yüksek Lisans, Mikro ve Nanoteknoloji

Tez Danışmanı: Prof. Dr. Raşit Turan

Ortak Tez Danışmanı: Doç. Dr. Görkem Günbaş

Ağustos 2019, 75 sayfa

Şu anda standart güneş hücreleriyle benzer pazar payına sahip Pasive Edilen Yayıcılı Arka Kontak (PERC) tipi güneş hücrelerinin sahip oldukları performans ve fiyat oranından dolayı yakın gelecekte fotovoltaik (PV) pazara hakim olması bekleniyor (ITRPV, 2019). Bu yüzden PERC üretim proseslerinin herbirinin optimizasyonu önem arz ediyor. PERC tipi güneş hücrelerinin arka yüzeyinde bulunan pasivasyon ve SiN_x tabakası, düşük öz dirence sahip kontaklar oluşturmak ve arka yüzeydeki toplam rekombinasyonu mümkün olduğunca azaltmak amacıyla lazer ile lokal olarak açılarak kontaklar oluşturulur. Bu sayede daha yüksek açık devre voltajı (V_{oc}) ve yük toplama verimi elde edilebilir. Bu tezdeki asıl odağı kontak oluşumu olan deneylerde 532 nm dalga boyuna sahip pikosaniye lazer kullanılarak lokal açıklıklar elde edildi. En iyi lazer parametresini belirlemek amacıyla fırınlamadan sonraki kontak genişlikleri, Al:BSF derinliği, void oluşma yüzdesi gibi özelliklerin lazer akışı ile arasındaki ilişki incelendi. Daha sonra bu özelliklerin güneş hücresi verimine etkilerini gözlemlemek ve optimum lazer akışı belirlemek amacıyla farklı lazer akışları kullanılarak üretilen güneş hücrelerinin birbirlerine göre verimleri incelendi. Ek olarak her bir lazer akışına karşılık gelen verimler Quokka simülasyonu ile hesaplandı. Bunların sonuçlarına

göre, Günam Fotovoltaik Hattı'nda (GPVL) üretilen PERC tipi güneş hücreleri için lazer prosesi optimize edilerek endüstriyel ölçekte %19 verim elde edildi

Anahtar Kelimeler: PERC tipi güneş hücreleri, Lazer prosesi, Arka kontak oluşumu, Arka kontak özellikleri

All dreamers

ACKNOWLEDGEMENTS

First and foremost, I would like to thank my supervisor, Prof. Dr. Raşit Turan for his great mentorship and accepting me as a member of GÜNAM. He was very supportive during my master and for my further academic career. During my MSc research, I have learned a lot from him not only in the field of science but also in professional life. Moreover, I would like to thank my committee members; Assoc. Prof. Dr. Alpan Bek, Asst. Prof. Dr. Ihor Pavlov, Asst. Prof. Dr. Selçuk Yerci, Asst. Prof. Dr. Veysel Ünsür for their valuable guidance and time. Also, I would like to thank my co-advisor Assoc. Prof. Dr. Görkem Günbaş for his support.

I would like to thank Fırat Es for his guidance that opens my mind and leads me every time. It was always enjoyable to talk to him about science and daily issues. I would like to continue my thanks with Deniz Türkay for his guidance to complete my MSc thesis. It was always a pleasure to discuss with him

I would like to thank Gamze Kökbudak for numerous PECVD procedure that she performed for me. She never turned me down and helped me as soon as possible. The biggest support in my experiments belongs to her. Another name that made my experiments possible is Emel Semiz. I would like to thank her for organizing my experiments and scientific discussions we made. Also, I am very thankful to all GPVL members: Efe Orhan, Gülsen Baytemir, Adem Yavuz, Gence Bektaş, Ahmet Keçeci, Sümeyye Koçak, Bülent Arıkan, Furkan for their contribution to my experiments. Moreover, I would like to thank Mona Zülfigari and Hisham Nasser for their help when I needed one.

Another thank you goes to Ali Erdoğan for his impactful motivation speeches. He was very supportive during my MSc education Huge thanks and appreciation go to my family and my friends for their full support during my entire education. Lastly, I gratefully acknowledge the funding received from the Scientific and Technological Research Council of Turkey (TUBITAK).

TABLE OF CONTENTS

ABSTRACT	v
ÖZ	vii
ACKNOWLEDGEMENTS	x
TABLE OF CONTENTS	xi
LIST OF TABLES	xiv
LIST OF FIGURES	xv
LIST OF ABBREVIATIONS	xviii
CHAPTERS	
1. INTRODUCTION	1
1.1. Fundamental Principles of Solar Cell Operation.....	1
1.1.1. Generation of Electrons and Holes	1
1.1.2. Formation of p-n Junction and Carrier Transport.....	2
1.1.3. Metal-Semiconductor Junction and Charge Collection	3
1.2. Basic Solar Cell Parameters	5
1.2.1. Short Circuit Current (I_{sc})	6
1.2.2. Open Circuit Voltage (V_{oc}).....	6
1.2.3. Fill Factor (FF).....	7
1.2.4. Efficiency (η)	8
1.3. Loss Mechanisms	8
1.4. PERC Type Silicon Solar Cells.....	12
1.4.1. Motivation.....	12
1.4.2. Literature Survey	13

2.	LASER PROCESS ON SILICON BASED SOLAR CELLS	21
2.1.	Laser Applications in PV Industry	21
2.2.	The Factors That Affect Laser Ablation Process	22
2.3.	Theoretical Background of Laser Ablation.....	23
3.	REAR CONTACT FORMATION IN PERC TYPE SOLAR CELLS	29
3.1.	Contact Formation Mechanism.....	29
3.2.	Void Formation Mechanisms.....	31
3.3.	The Mathematical Models for the Al:BSF Depth.....	32
4.	DEVICE FABRICATION	39
4.1.	Fabrication Procedure for the Study “Effects of the Pitch on Solar Cell Performance”	40
4.1.1.	Wet Chemical Steps: Texturing and Cleaning	40
4.1.2.	Doping	40
4.1.3.	Single Side Etching (SSE).....	41
4.1.4.	Plasma Enhanced Chemical Vapor Deposition (PECVD).....	41
4.1.5.	Laser Ablation	42
4.1.6.	Metallization and Firing	43
4.2.	Fabrication Procedure for the Study “Effects of Laser Parameters on Contact Formation and Solar Cell Performance”	45
4.2.1.	Laser Ablation and Characterization Process.....	46
4.2.1.1.	Innolas Picosecond Laser System used in the Studies.....	46
5.	RESULTS AND DISCUSSIONS	51
5.1.	The Effects of Firing Profiles on BSF Formation and Solar Cell Performance	51
5.2.	The Effects of the Pitch on Solar Cell Parameters.....	54

5.3. Laser Ablation Properties	55
5.4. The Effects of the Laser Parameters on Contact Behaviours	57
5.5. The Effects of Laser Parameters on Solar Cell Performance	61
6. CONCLUSIONS	67
REFERENCES.....	70

LIST OF TABLES

TABLES

Table 1.1. Properties of n-type and p-type materials.....	2
Table 4.1. Ingredients of the Al paste.....	44
Table 4.2. Applied firing profiles	45
Table 4.3. Applied Laser Parameters.....	50
Table 5.1. Contact Characteristics such as max Al:BSF depth and void percentage for 50 and 70 μm contact width cases	55
Table 5.2. Tabulated results of the experiment for 1 mm contact pitch case	58
Table 5.3. Input parameters utilized for Quokka simulation.....	63
Table 5.4. Solar cell performance of the best sample.....	65

LIST OF FIGURES

FIGURES

Figure 1.1. (a) Schematics of the p-n junction showing the depletion region and its charge content (b) p-n junction energy band diagram at thermal equilibrium.....	2
Figure 1.2. For Schottky junction case, energy band diagrams for n- type and p-type semiconductors before joining (a)-(c) and at equilibrium (b)-(d). For the ohmic junction case, energy band diagram for n-type and p-type semiconductor before joining (e)-(g) and at equilibrium (f)-(h).....	4
Figure 1.3. The impacts of diffusion length, surface passivation and the distance from the junction on the collection probability.....	5
Figure 1.4. I-V curve at dark and under illumination	5
Figure 1.5. I-V and P-V curve of a solar cell.....	6
Figure 1.6. Loss mechanisms that determines the Shockley Queisser limit (at AM1.5 spectrum) (Smets et al., 2016).....	8
Figure 1.7. Estimation of the R_{sh} and R_s from the I-V curve	11
Figure 1.8. Market share of different type of solar cells based on ITRPV report published in 2019 (ITRPV, 2019).....	13
Figure 1.9. Standard solar cell vs PERC type solar cell.....	14
Figure 1.10. The first introduced PERC structure (Blakers & Green, 1986).....	14
Figure 1.11. Simplified process sequence that is generally applied in the PV industry	16
Figure 1.12. The cross-section SEM images of filled contact (a) partial void (b) complete void (c) (Kranz et al., 2016)	18
Figure 2.1. The absorption coefficient and corresponding absorption depth as a function of wavelength for Silicon material.....	22
Figure 3.1. Al-Si phase diagram	29

Figure 3.2. Illustration of the rear contact formation for the homogenous and LCO case. Si concentration in the Al paste is represented by the curve while Si solubility according to temperature is represented by the dash line. (Lauermann et al., 2015) 31

Figure 3.3. Illustration of assumed contact geometry that shows h and Δ values..... 33

Figure 3.4. The ratio of m_{Al} / A for different contact geometries: full area, line, point. Here, contact width after firing is denoted by a..... 34

Figure 3.5. Simplified firing model according to time 36

Figure 4.1. Simplified process sequence of the experiments..... 39

Figure 4.2. Illustration of the PECVD system from top view 42

Figure 4.3. The laser ablation design of the experiment..... 43

Figure 4.4. (a) Illustration of the Innolas Picosecond Laser System and (b) scheme that shows the relation between assemblies..... 47

Figure 4.5. Principle function of EOM..... 47

Figure 4.6. Illustration that shows the correlation between the polarization and fast high voltage signal..... 48

Figure 4.7. Correlation between high voltage signal and pulses 48

Figure 4.8. Schematic design of the laser system..... 49

Figure 4.9. Measured power values according to frequency (a) and motor positions when 1 MHz frequency was used (b) and 200 kHz frequency was used (c)..... 49

Figure 5.1. SEM images of the rear contacts that shows BSF depths for the firing profiles which are (a) standard (b) 300-450-850-850-850-930 (c) 300-650-850-850-850-930 (d) 300-750-850-850-850-930 (e) 450-750-850-850-850-930 were applied. 52

Figure 5.2. I-V results of the 25 samples..... 53

Figure 5.3. (a) SEM images of the front fingers (b) average of the front finger widths for each wafer 53

Figure 5.4. Calculated surface recombination velocity values according to with min BSF thickness from study (S. Gatz et al., 2012)..... 54

Figure 5.5. I-V results..... 54

Figure 5.6. SEM image of an ablated area when 1.8 J/cm ² fluence is used and optic image of an ablated area when 4.2 J/cm ² fluence is used	56
Figure 5.7. The relation between LCO width and fluence.	56
Figure 5.8. An example SEM image for filled contact (a) partial void contact (b) void contact (c).....	57
Figure 5.9. EDAX line analysis on the Al paste	58
Figure 5.10. Contact width and max BSF depth values for each fluence. Lines are given for the visual aid.....	59
Figure 5.11. An example SEM image of a partial void	59
Figure 5.12. Void fraction relation with fluence and LCO width. The lines are given for the visual aid.....	60
Figure 5.13. Si lateral distribution in the Al paste over the position to LCO according to time dependent spread (σ) that are presented with the color coding (Lauermann, 2016).	60
Figure 5.14. PL images that shows scratches (mechanical damage) on a wafer (a) and non-uniform passivation (b). Color bar shows the average life time values in terms of μ s.....	61
Figure 5.15. Front finger SEM images that indicates non-uniform spread of silver which are 312 μ m (a) and 212 μ m (b).....	61
Figure 5.16. Efficiency results according to laser fluence when 1mm, 1.5 mm and 2 mm pitch is applied.	62
Figure 5.17. Calculated efficiency results with identical doping profile assumption (a) and when doping profile changed for fluence 4.2 J/cm ² (b) for 1 mm pitch case.	64
Figure 5.18. Calculated efficiency results when doping profile changed for fluence 4.2 J/cm ² for 1.5 and 2 mm pitch cases	64
Figure 5.19. SEM images when fluence was 4.2 J/cm ² (a) and 1.8 J/cm ² (b). The heat-affected zone is highlighted in green.	65

LIST OF ABBREVIATIONS

ABBREVIATIONS

AM	Air Mass
Ag	Silver
Al	Aluminum
ARC	Anti-reflection coating
BSF	Back surface field
CB	Conduction band
c-Si	Crystalline silicon
CO ₂	Carbon dioxide
Cz	Czochralski
E _{M,F}	Metal fermi level
eV	Electron volt
FF	Fill factor
FZ	Float-Zone
G	Photo generation rate
GW	Gigawatt
HF	Hydrofluoric
IBC	Interdigitated-back-contact
I ₀	Dark saturation current
I _L	Light generated current

I_{SC}	Short circuit current
I-V	Current-Voltage
J	Current density
J_{MPP}	Current density at maximum power point
J_0	Dark saturation current density
J_{SC}	Short circuit current density
kW	Kilowatt
L_D	Diffusion length
MS	Metal-Semiconductor
MW	Megawatt
N_0	Photon flux
N_D	Doping concentration
PECVD	Plasma enhanced chemical vapor deposition
PV	Photovoltaic
R_C	Contact resistance
RCA	Radio corporation of America
R_S	Series resistance
R_{SH}	Shunt resistance
SiN_x	Silicon nitride
SiO_2	Silicon dioxide
SRH	Shockley-Read-Hall
SQ	Shockley-Queisser

Ti/Pd/Ag	Titanium/Palladium/Silver
V	Voltage
VB	Valence band
V_{bi}	Built-in potential
V_{MPP}	Voltage at maximum power point
V_{OC}	Open circuit voltage
W_{FM}	Metal work function
WFSC	Semiconductor work function
QSSPC	Quasi-steady-state photoconductance
ρ_c	Specific contact resistivity
q	Elementary charge
η	Cell conversion efficiency
Φ_B	Schottky barrier height

CHAPTER 1

INTRODUCTION

1.1. Fundamental Principles of Solar Cell Operation

The operation of the solar cell relies on photon absorption, photo-generation, separation and collection of the generated electrons (e) – holes (h). Briefly, the absorption of the light makes an electron to raise the higher energy level and creates electrons and holes that need to be spatially separated from each other, and collected by an external contact to generate current and voltage.

1.1.1. Generation of Electrons and Holes

Generation of e-h pair means exciting an electron from valance band (VB) to the conduction band (CB) while leaving a hole behind. The minimum energy required to create an electron-hole pair is equal to the bandgap energy (E_g) which is specified as the difference between the highest energy level of the valence band and lowest energy level of the conduction band. The excitation of an electron from the valence band to the conduction band can occur by lattice vibration or photon absorption. For the solar cells, we need photon absorption to create higher powers. If the material has impurities the excitation can be attained in several steps. For instance, firstly electron is raised to impurity level and then to the valence band.

The probability of the photon absorption is related to the density of empty energy levels in the conduction band and occupied energy levels in the valence band, and during the change of occupation energy and momentum should be conserved.

Moreover, absorption depth, which depends on the absorption coefficient (α) of the material and wavelength of the incoming photon, should be taken into consideration.

For instance, photons with higher energies such as blue light are absorbed near the surface.

1.1.2. Formation of p-n Junction and Carrier Transport

The doping process is performed to make a semiconductor substrate p-type or n-type. The properties of the p-type and n-type materials are presented in Table 1.1.

Table 1.1. *Properties of n-type and p-type materials*

	<i>n-type</i>	<i>p-type</i>
Dopant	Group V	Group III
Bonds	Excess electrons	Excess holes
Majority Carriers	Electrons	Holes
Minority Carriers	Holes	Electrons

When p-type and n-type materials are brought together, electrons and holes diffuse to the opposite side and recombine each other, and then fixed ionized atoms left behind create an electric field with the direction from n-side to p-side. This electric field prevents further recombination when the Fermi level equilibrium is reached. The carrier-free area is called the depletion region which is shown in Figure 1.1a. Moreover, drift current that depends on the electric field is generated through the junction. Figure 1.1b shows the energy band diagram for the p-n junction. The band bending shown in Figure 1.1b and electric field strength depends on the Fermi level difference between p-type and n-type material. In the solar cell, close to the junction drift mechanism dominates where bulk conditions are dominant away from the junction.

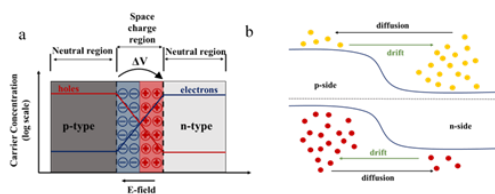


Figure 1.1. (a) Schematics of the p-n junction showing the depletion region and its charge content (b) p-n junction energy band diagram at thermal equilibrium

1.1.3. Metal-Semiconductor Junction and Charge Collection

When metals and semiconductors that have different work functions are brought together, a charge transfer takes place until the fermi levels line up at equilibrium. Two types of junction are possible: Schottky junction (rectifying), Ohmic junction (non-rectifying).

Band diagrams of these two junction types are shown in Figure 1.2 before and after the junction formation for different cases. In the case of Schottky junction (Figure 1.2b, d), current flows in one direction from semiconductor to metal when positively biased (forward bias) whereas the so-called Schottky barrier blocks the current flow from metal to semiconductor side. For the ohmic junctions shown in Figure 1.2f and h, the charge flow takes place equally in both directions independently from the polarity of the applied voltage. In solar cells, ohmic contacts having a low contact resistance are desirable to ensure an easy charge collection from both p- and n-side of the solar cell. Ohmic junction behavior is obtained either by band alignment with proper metal choice as illustrated in Figure 1.2 or by using heavy doping in the semiconductor side. Heavy doping makes the Schottky barrier region thin enough so that current flow can take place by easy tunneling through the barrier in both directions.

The collection probability of generated carriers by light absorption depends also on the surface passivation, diffusion length and the distance from the junction. For instance, the collection probability of e-h pairs generated away from the junction farther than diffusion length or close to the surface with poor passivation is very low. The impacts of these properties are shown in Figure 1.3. The light generated current density (J_L) can be calculated from the integration of multiplied generation rate $G(x)$ with collection probability (CP) at a particular position over the wafer thickness (W) as in Eqn. 1.1.

$$J_L = \int_0^W G(x)CP(x) dx \quad (1.1)$$

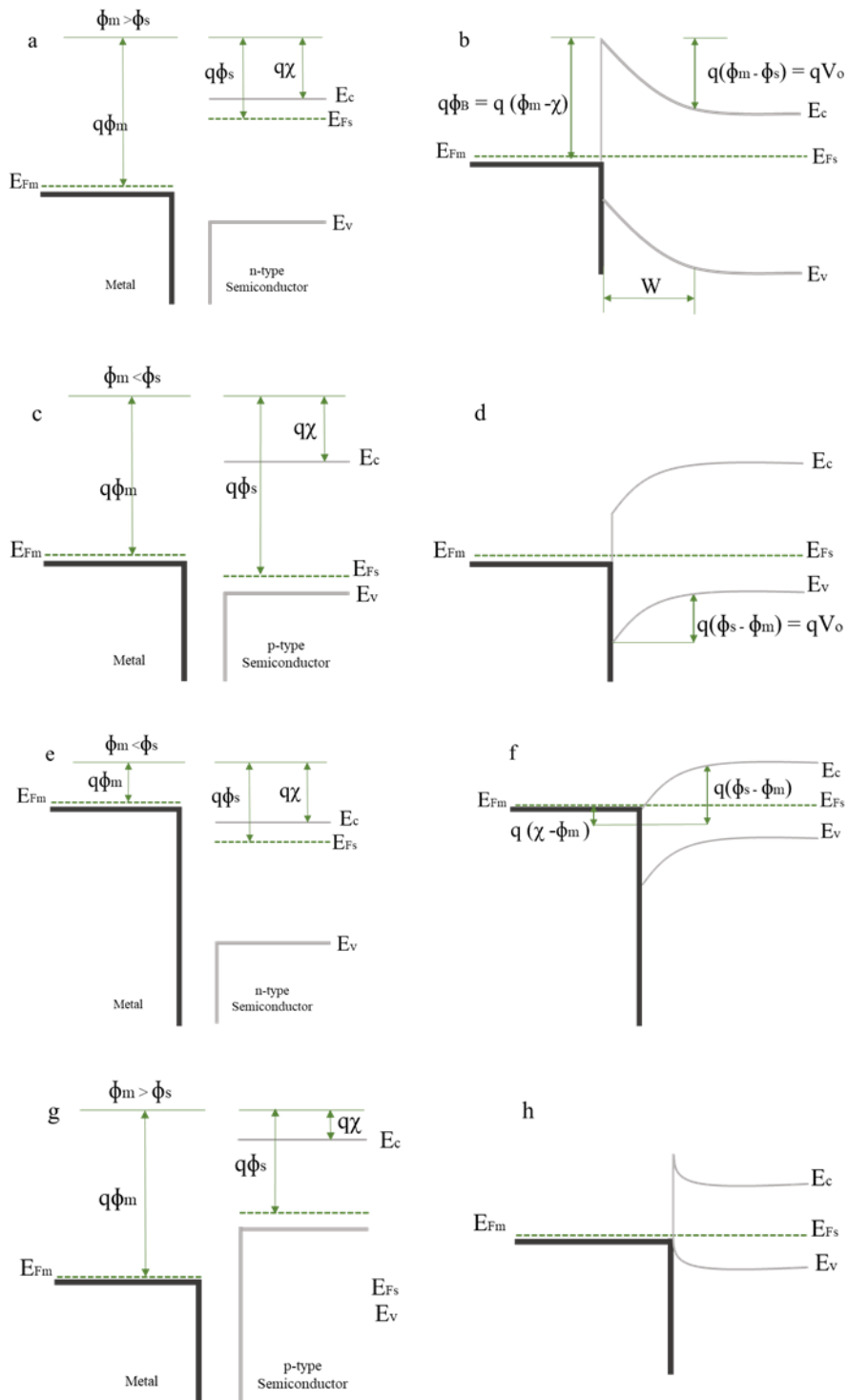


Figure 1.2. For Schottky junction case, energy band diagrams for n- type and p-type semiconductors before joining (a)-(c) and at equilibrium (b)-(d). For the ohmic junction case, energy band diagram for n-type and p-type semiconductor before joining (e)-(g) and at equilibrium (f)-(h).

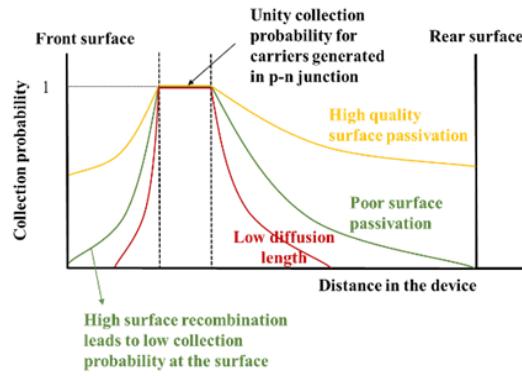


Figure 1.3. The impacts of diffusion length, surface passivation and the distance from the junction on the collection probability

1.2. Basic Solar Cell Parameters

Solar cell performance is determined by the current-voltage (I-V) characterization. Solar cells act as a diode under the dark. However, the I-V curve of the diode equation shifts under the illumination (Figure 1.4) along the y-axis, the light generated current (I_L) is added to the diode equation and the diode equation becomes:

$$I = I_L - I_0 \left[\exp\left(\frac{qV}{nkT}\right) - 1 \right] \quad (1.2)$$

Here, I_0 is dark saturation current, the elementary charge is denoted by q , Boltzmann constant is shown by k , T is the cell temperature.

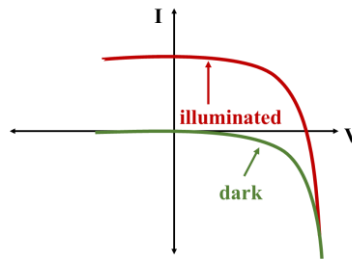


Figure 1.4. I-V curve at dark and under illumination

Eqn. 1.2 can be expanded to following equation considering the parasitic resistances which are series resistance (R_s) and shunt resistance (R_{sh}).

$$I = I_L - I_0 \left(e^{\frac{q(V+IR_s)}{nkT}} - 1 \right) - \frac{V + IR_s}{R_{sh}} \text{ where } n \text{ is ideality factor} \quad (1.3)$$

More specifically, I-V curve ranges between I_{sc} and V_{oc} as in Fig.1.5 and solar parameters showing on Fig.1.5 are explained following sections.

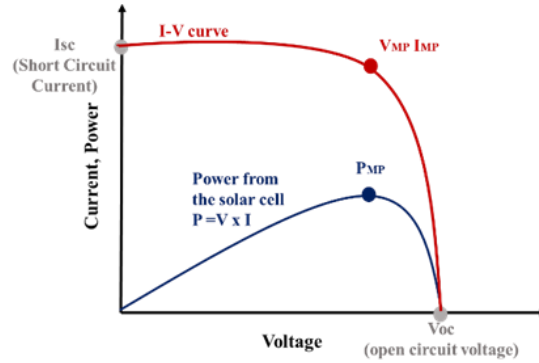


Figure 1.5. I-V and P-V curve of a solar cell

1.2.1. Short Circuit Current (I_{sc})

The short circuit current (I_{sc}) is defined as the current value when the voltage is zero. In an ideal solar cell with moderate resistive losses, I_L and I_{sc} are the same. Hence, it is the maximum current that can be obtained. Short circuit current is affected by incoming light intensity and spectrum, solar cell area, optical properties of the device, collection probability.

1.2.2. Open Circuit Voltage (V_{oc})

Open circuit voltage (V_{oc}) can be defined as the voltage value when the current is zero and accordingly maximum voltage that can be obtained from a solar cell. The open-circuit voltage formula calculated from Eqn 1.2 by putting zero instead of the current value (I), is as follows:

$$V_{oc} = \frac{nkT}{q} \ln \left(\frac{I_L}{I_0} + 1 \right) \quad (1.4)$$

At first view, it may seem that V_{oc} increases with increasing temperature. However, I_0 also depends on the temperature due to variation of intrinsic carrier concentration, which leads to drop in V_{oc} . Since I_0 is dominant, V_{oc} decreases with temperature

increment. Moreover, I_0 is also affected by recombination, leading to that V_{oc} strongly depends on recombination.

Also, V_{oc} can be calculated from intrinsic doping concentration (n_i) as shown in the following equation:

$$V_{oc} = \frac{kT}{q} \ln \left[\frac{(N_A + \Delta n)\Delta n}{n_i^2} \right] \quad (1.5)$$

Here, kT/q represents the thermal voltage, the doping concentration is denoted by N_A , and excess carrier concentration is Δn .

1.2.3. Fill Factor (FF)

Fill Factor (FF) is the ratio of maximum power (P_{MP}) obtained from solar cell to product of V_{oc} and I_{sc} as shown below:

$$FF = \frac{P_{MP}}{V_{OC} \times I_{SC}} \text{ where } P_{MP} = V_{MP} I_{MP}$$

Max theoretical FF can be obtained by taking derivative of the power with respect to voltage where it is equal to zero:

$$\frac{d(IV)}{dV} = 0 \quad (1.6)$$

Which results in;

$$V_{Mp} = V_{OC} - \frac{nKT}{q} \ln \left(\frac{qV_{MP}}{nkT} + 1 \right) \quad (1.7)$$

Here, extra steps are needed to reach max FF and also Lambert functions should be solved. However, an empirical relation between FF and V_{oc} was shown as follows:

$$FF = \frac{V_{oc} - \ln(V_{OC} + 0.72)}{V_{OC} + 1} \quad (1.87)$$

In both Eqn 1.7 and 1.8, the effects of parasitic resistances are neglected. In practice, the real FF values are lower due to resistive losses. Hence, FF is usually obtained from I-V curve.

1.2.4. Efficiency (η)

For any system, efficiency is defined as the ratio of output power to input power. Since $P_{mp} = V_{oc}I_{sc}FF$, the efficiency of a solar cell can be written as:

$$\eta = \frac{V_{oc}I_{sc}FF}{P_{in}} \quad (1.9)$$

Under standard test conditions, input power is taken as 100 mW/cm^2 for the calculations. The conditions such as intensity and spectrum of incoming light, the temperature should be carefully controlled to make a reliable comparison between the cells.

1.3. Loss Mechanisms

The maximum efficiency that can be obtained by a single p-n junction solar cell is called the Shockley–Queisser (SQ) limit. For instance, a single p-n Junction solar cell with 1.4 eV bandgap can have a maximum 33.7% efficiency at AM 1.5 solar spectrum (Smets, et al., 2016). The parameters that limit efficiency are given in Figure 1.6.

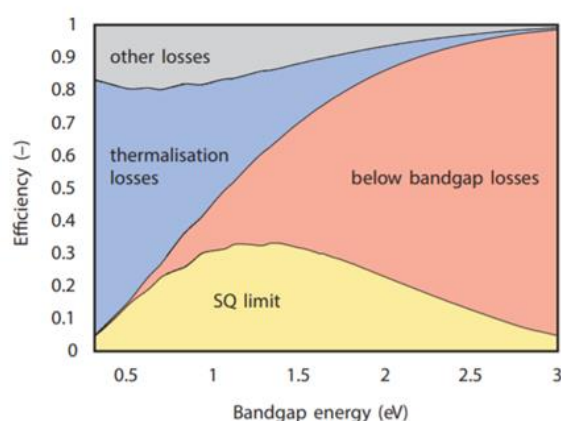


Figure 1.6. Loss mechanisms that determines the Shockley Queisser limit (at AM1.5 spectrum) (Smets et al., 2016)

The main losses are caused by below bandgap photons that cannot be absorbed. Also, the photons with above bandgap energy affect the device performance due to the relaxation of the carriers at the conduction band and valance band edges. Further, the radiation comes from the sun cannot be totally captured by the solar cell at room temperature. Also, the tradeoff between low radiative recombination and high voltage is another loss mechanism that is termed as other losses.

However, the real efficiencies are less than the theoretical limits due to further intrinsic losses.

I_{sc} losses

Optical losses have a significant impact on the short circuit current loss. For instance, top fingers and reflection of the incident light at the surface reduces the light absorption and therefore carrier generation, which leads to I_{sc} loss. Another example is that if the cell is not thick enough, some of the incident light may transfer through. Also, recombination in the bulk and surface results in lower collection probability and hence it has a significant impact on the I_{sc} loss. Lastly, series resistance should be reduced as possible to have higher I_{sc} values.

V_{oc} Losses

The main reason for the open-circuit voltage loss is recombination. The following should be taken into consideration to reduce recombination.

- o Minimized minority carrier concentration at equilibrium reduces the recombination. This can be attained by increasing the doping level.
- o High diffusion length, which depends on applied wafer processes, the material itself and doping, is required. The higher doping level results in smaller diffusion length, leading to a trade-off between diffusion length and minority carrier recombination.
- o Surface passivation reduces the recombination at the surfaces and enables higher V_{oc}. Since the passivation layers are usually dielectric materials, it cannot be used at ohmic contacts. As a solution, recombination can be reduced by increasing the doping

level under the contacts. For instance, high doped BSF layers act as like a p-n junction and introduce a barrier to the minority carriers. Hence it has a net effect on the passivation.

o Trapping levels should be minimized.

There are three main recombination types which are called Radiative, Shockley-Read-Hall (SRH) and Auger. In radiative recombination, an electron from conduction band recombines with a hole and emits a photon. On the other hand, SRH is a two-step process where electrons are captured by forbidden energy states (formed due to defects) and then recombines with a hole. In Auger recombination, the resulted energy is given to another carrier in the conduction band before electron in the CB combines with a hole in VB. It is dominant when the materials have a high impurity level and high doping concentration. SRH and Auger are more dominant for silicon solar cells due to the indirect bandgap nature of silicon.

FF Losses

Resistive losses and recombination affect the fill factor. The major impact come from the parasitic resistances which are series resistance (R_s) and shunt resistance (R_{sh}).

The series resistance results from the current movement in the base and junction, interface between metal and the semiconductor, metal contacts. An easy method to obtain series resistance is finding the slope of the I-V curve at V_{oc} (Figure 1.7).

The relation between FF and R_s can be obtained by the assumption of that maximum power equals the maximum power when there is no R_s minus the hidden power due to R_s . Accordingly, the equation can be written as:

$$P'_{MP} \sim V_{MP} I_{MP} - I_{mp}^2 R_s = P_{MP} \left(1 - \frac{I_{sc}}{V_{oc}} R_s \right) \quad (1.10)$$

Where V_{oc}/I_{sc} is approximated as characteristic resistance (R_{CH}) and normalized resistance is defined as $r_s = R_s/R_{CH}$. Hence, the equation become:

$$P'_{MP} = P_{MP}(1 - r_s) \quad (1.11)$$

If the effects of series resistance on the V_{oc} and I_{sc} are neglected, the relation between FF and R_s become:

$$V'_{OC}I'_{SC}FF' = V_{OC}I_{SC}FF(1 - r_s) \quad (1.12)$$

$$FF' = FF (1 - r_s) \quad (1.13)$$

A slightly more accurate formula was presented according to empirical results.

$$FF' = FF (1 - 1.1r_s) + \frac{r_s^2}{5.4} \text{ when it is valid for the cases of } r_s < 0.4 \text{ and } V_{oc} > 10 V \quad (1.14)$$

The shunt resistance (R_{SH}) results from defects in the material and leads to power loss due to alternative paths created for the light generated current. The shunt resistance can be estimated from the slope of the I-V curve at I_{sc} point (Figure 1.7) and its destructive effect can be observed more clearly under the low light level.

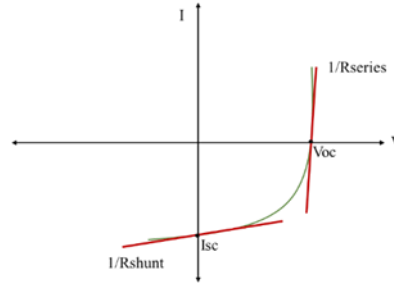


Figure 1.7. Estimation of the R_{sh} and R_s from the I-V curve

The relation between FF and shunt resistance can be obtained with a similar approach done the relation between FF and R_s . The maximum power can be estimated as the maximum power when there is no shunt resistance minus the power loss caused by shunt resistance. Then the relation between the FF and R_{SH} can be reached by following the steps that are shown below:

$$P'_{MP} = V_{MP}I_{MP} - \frac{V_{MP}^2}{R_{SH}} = V_{MP}I_{MP} \left(1 - \frac{V_{MP}}{I_{MP}} \frac{1}{R_{SH}} \right) = P_{MP} \left(1 - \frac{V_{OC}}{I_{SC}} \frac{1}{R_{SH}} \right) \quad (1.15)$$

$$P'_{MP} = P_{MP} \left(1 - \frac{R_{CH}}{R_S}\right) \quad (1.16)$$

$$P_{MP} = P_{MP} \left(1 - \frac{1}{r_{SH}}\right) \text{ since } r_{SH} = \frac{R_{SH}}{R_{CH}} \quad (1.17)$$

$$FF' = FF \left(1 - \frac{1}{r_{SH}}\right) \quad (1.18)$$

Let's denote FF' as FF_{SH} and the FF value that is independent of shunt resistance as FF_0 . Again, a more accurate empirical approximation was obtained for the relation between FF and R_{SH} as:

$$FF_{SH} = FF_0 \left(1 - \frac{V_{OC} + 0.7 FF_0}{V_{OC} r_{SH}}\right) \text{ when it is valid if } r_{SH} > 0.4 \quad (1.19)$$

1.4. PERC Type Silicon Solar Cells

1.4.1. Motivation

It is a well-known fact that global warming is a big threat to humanity and results from carbon dioxide (CO_2) released during the combustion of fossil fuels. Most of the energy demand is supplied by fossil fuels and it is estimated that energy consumption will grow by %25 until 2040 (IEA, 2018). Hence cleaner solutions, such as renewable energy, are needed. However, the use of renewable energy sources like solar and wind energy has been limited due to high cost and some technical limitations. Thanks to the intensive R&D activities and increase in volume production, the cost of the energy generation has fallen to very competitive levels in recent years. The share of renewable energy in electric power generation, which is %25 in 2018, is expected to be over %40 until 2040 (Lacey, 2018). In particular, photovoltaic (PV) technology is very promising since it uses the sun as a source.

99 GW PV installation in 2017 and 104 GW PV installation in 2018 have been achieved (Munsell, 2018). The total cumulative PV capacity has exceeded 500 GW at the end of 2018 and expected to reach 1 TW by 2023 (Lacey, 2018).

Ever since the proposal of largescale solar cells, the standard crystalline Si solar cells have dominated the growing PV industry until recently. However, today PERC type c-Si solar cells have a similar market share compared to standard type solar cells and it is expected that PERC will be the dominant type of the PV market (ITRPV, 2019) since higher efficiencies than that of standard type can be achieved with a similar cost.

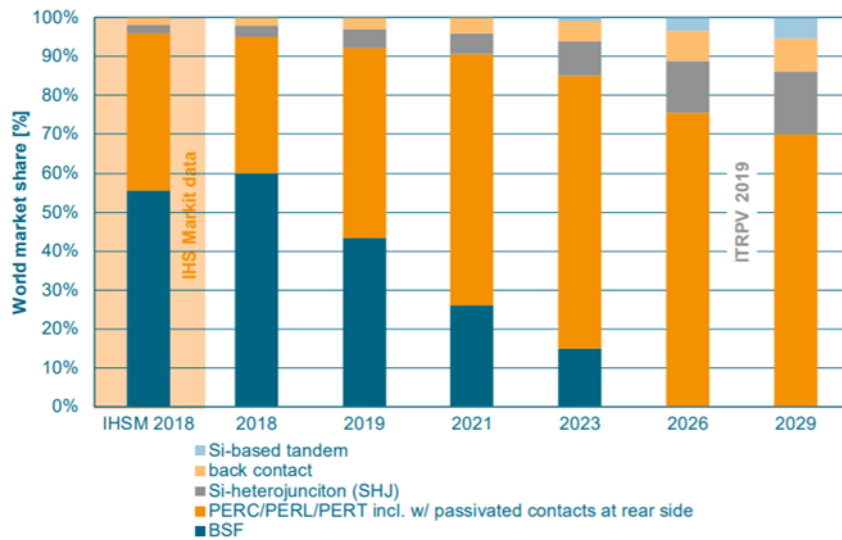


Figure 1.8. Market share of different type of solar cells based on ITRPV report published in 2019 (ITRPV, 2019)

1.4.2. Literature Survey

PV industry has been dominated by the standard type solar cells for a long time. However, the full Al layer at the rear side causes recombination of the photo generated carriers and partly IR light absorption, which limits the solar cell efficiency around %20. To overcome these loss mechanisms, PERC type solar cell was introduced in 1986 (Blakers & Green, 1986). Basically PERC type solar cells include a passivation layer and SiN_x capping layer at the rear side and collection of the photo-generated carriers is attained through openings on the layers (Figure 1.9). In this way, the recombination at the rear surface is reduced and light trapping properties are improved. Since the first introduction of the PERC structure, companies and research institutes have been developed low-cost processes that achieve higher efficiencies

especially for the rear contacts and the rear passivation layer, which made PERC type solar cells production feasible and cost-effective for the industry. In this part, the progress of the PERC type Si solar cell especially related to rear contacts will be discussed.

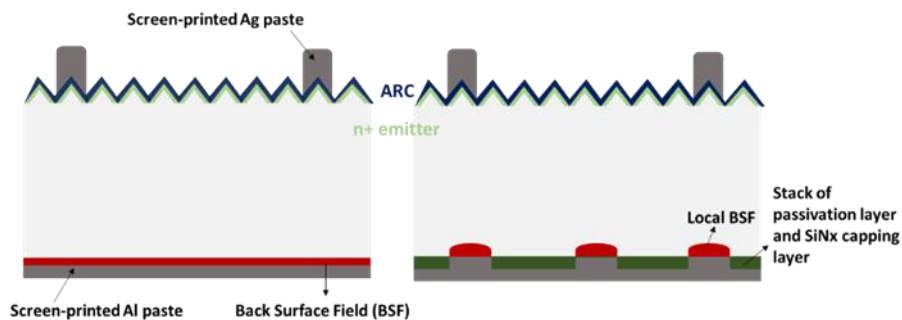


Figure 1.9. Standard solar cell vs PERC type solar cell

Historical Development

The PERC structure first appeared in the paper of Blakers et al in 1989 (Blakers & Green, 1989) whereas it was first described in UNSW final grant report in 1983 (Green, 2015). For the first lab-scale PERC Si solar cell, the thermally grown SiO₂ layer was used on the rear side of the p-type FZ Si base and locally opened by lithography in a point shape. Then, Al was evaporated to form the rear metal contacts. On the other hand, for the front side of the Si base, several oxide masking and photolithography steps were performed to form inverted pyramids before phosphorous doping and TiPdAg front contact formation. The illustration of this PERC structure is given in Figure 1.10.

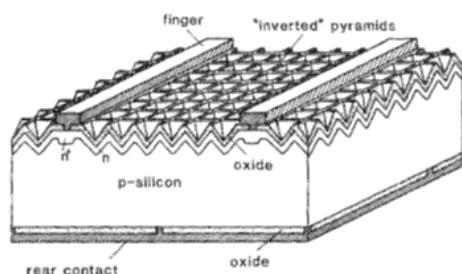


Figure 1.10. The first introduced PERC structure (Blakers & Green, 1986)

In the following years, passivated emitter and rear locally diffused (PERL) concepts were introduced (Zhao et al., 1997) and became world record efficiency silicon solar cells for a long time. Process and technology developments regarding passivation layers, local contact openings, and metallization made these structures cost-efficient.

Instead of a lab-type thermally grown oxide layer, which is not cost-effective and resulted in degradation of bulk carrier lifetime during the high-temperature process, alternative materials and processes for rear passivation layer were investigated. For a while, SiN_x layer by PECVD was thought as promising candidate since it was already applied to the front side as a passivation layer and ARC (Schmidt et al., 2001). However, fixed positive charges of the SiN_x layer lead to increase in recombination. On the other hand, aluminum oxide exhibits negative fixed charges and hence was found to be an applicable candidate for the passivation (Agostinelli et al., 2006). Over the years high throughput devices such as PECVD (Hofmann et al., 2009; Schmidt et al., 2001) and spatial ALD (Werner et al., 2011) were developed for the aluminum oxide passivation layer. In addition, using SiN_x as a capping layer on top of the aluminum oxide provided resistance to the Al paste during firing with enhancement in optical reflectivity properties at the rear surface that accordingly increase IR light absorption (Kray et al., 2008; Veith et al., 2011).

Another promising development was achieved by the Preu et al. (Preu et al., 2000) showing that the laser ablation process can be used instead of lab-type photolithography for LCO step. Preu et al. used thermal evaporated Al as metal contact. Later on, the rear contact formation process was improved by combining laser ablation step with screen printed metallization by Agostinelli et al. (Agostinelli et al., 2005). This approach enabled higher efficiencies of solar cells in large scale that exceeds the efficiencies of corresponding conventional solar cells. Further, optimized line shape local contacts were applied by Gatz et al for the first time in 2011 and achieved %19.4 solar cell efficiency which was the record of its time (Sebastian Gatz et al., 2011).

Also, alternative techniques for the contacts such as laser fired contacts (LFC) (Preu et al., 2002) and nickel-copper plating contact (Tous et al., 2013) were studied. Although these approaches showed bright results, they have not applied to the industry due to process complexity of the plating and thinner Al-BSF layer resulted from the LFC process compared to screen-printing.

Another factor that should be taken notice is that phosphorus doping should not be present at the rear side. This can be achieved by the Centaurus process (Münzer et al., 2012) and single side etching after the doping (Cornagliotti, Tous, & Russell, 2012).

The mainstream PERC fabrication process that is usually applied in today's industry after these improvements are given in Figure 1.11.

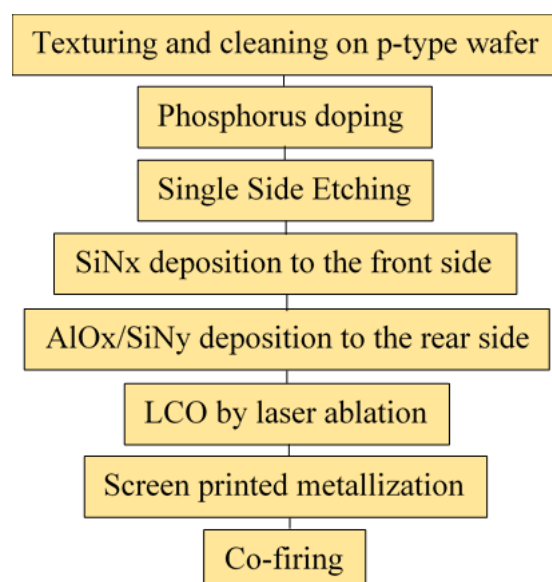


Figure 1.11. Simplified process sequence that is generally applied in the PV industry

Rear Contact Formation

Local contact opening (LCO) in which the stack of the passivation layer and capping layer are locally opened should be performed before the metallization to form low recombination and low resistive contacts. In this way, the total recombination at the rear side of the wafer is significantly reduced, leading to a higher open-circuit voltage

and charge collection efficiencies in the base of the cell. Here, the LCO and metallization are the key steps for the rear contact formation.

As mentioned, LCO process for the first produced lab-type PERC structure was achieved by the photolithography before the thermal evaporation of Al for rear metallization (Blakers & Green, 1986).

As an alternative contact formation sequence, etching paste before the screen printing process of Al was applied (Stockum & Rohatgi, 2006). Screen-printed etching paste was thermally activated to achieve the LCO and the remaining of it was removed by wet chemical cleaning. Subsequent to these processes Al was screen printed to the sample and fired to form Al-Si eutectic alloy.

Another approach that is called Laser Fired Contacts (LFCs) in which Al paste was screen printed or evaporated and locally subjected to pulsed laser was introduced by Preu et al. (Preu & Lu, 2002). In this way, over 18% efficiency of industrial PERC cell was achieved for the first time (Gautero et al., 2009) and, later efficiencies up to %20 (Zimmermann et al., n.d.). However, LCO approach seemed more promising since the Al-BSF depths were much deeper compared to ones of LFCs (~1 μm), leading to reduction of carrier recombination and correspondingly increase in cell efficiencies. Compared to three-step etching paste, one step LCO process is more cost-effective and can be performed by laser ablation. Hence laser ablation become industry's favorite and widely investigated (Ali et al., 2019; J. Kim et al., 2014; M. Kim et al., 2013)

After LCO step, front and rear contacts are formed with screen printed metallization followed by the single-step co-firing process, which leads to structures on the backside as shown in Figure 1.12. In this configuration, parameters such as rear contact fraction and pitch, LCO geometry and dimensions, local back surface field (BSF) depth and void presence are some of the parameters that affect the fill factor and V_{oc} of the fabricated cell thereby changing recombination and series resistance of the cell. The effects of the mentioned contact behaviors will be discussed in the next section.

Contact Behaviors

During the firing process, inter diffusion of the Al and Si form the rear contacts which can be assigned by one of the three categories: filled contact, partial void, complete void (see Figure 1.12).

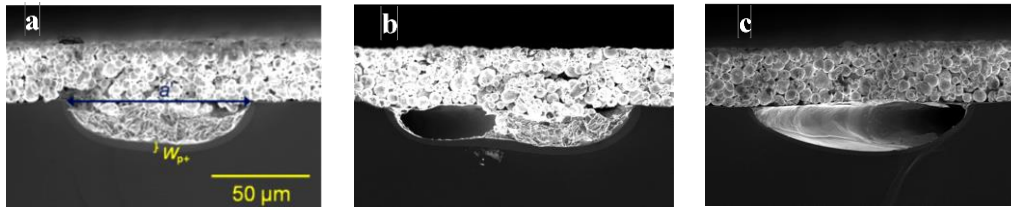


Figure 1.12. The cross-section SEM images of filled contact (a) partial void (b) complete void (c) (Kranz et al., 2016)

As it is seen in the image (Figure 1.12a), the ' W_p ' represents the Al-BSF thickness and ' a ' is the contact width which is wider than LCO width due to Si-Al inter diffusion during the firing.

Although the rear contacts of first introduced PERC structure had a point shape, afterward it was demonstrated that the point-shaped contacts in industrial-scale have higher void formation rate compared to line-shaped contacts, leading to variation of Al-BSF depth between 0-6 μm where it was 4-7 μm for line-shaped contacts. This results in increase in local rear contact recombination and decrease in cell efficiencies (Lauer mann, 2016). Also lifetime measurements have shown that lower rear contact recombination velocities can be achieved with line-shaped contacts (Müller et al., 2011). Further, Gatz et al demonstrated that Al-BSF depth gets deeper as the contact width increases until a point and surface recombination velocities can be lowered to 300 cm/s (S. Gatz, Müller, Dullweber, & Brendel, 2012).

Urrejola et al (Urrejola, Peter, Plagwitz, & Schubert, 2011) studied the contact formation mechanism and examined the lateral diffusion of Si from the base in the Al paste during the firing process. Basically, the founding was that the lateral distributions were varied from 300 μm to 1000 μm dependent on the peak firing

temperature and LCO width. As a side note, the line-shaped LCO was used for this study.

Based on all of these results, a mathematical model for the calculation of Al-BSF depth was proposed (Müller, Bothe, Gatz, & Brendel, 2012) by assuming box-shaped eutectic contacts with homogenous lateral distribution of Si in Al paste after firing. The homogenous profile was chosen for the simplification reasons instead of the Gaussian profile requiring to solve differential equations.

Later, the model was extended by incorporating differential equations, which allows more accurate silicon distribution calculation in Al paste (Lauermann et al., 2015). These models were explained very explicitly in “The Mathematical Models for the BSF depth” section in Chapter 3. However, these models do not specify the effects of the voids on the p+ layer. The studies related to void issue showed that void presence can vary the Al-BSF depth range from no BSF to BSF depth the same with one of the filled contacts (Chen et al., 2014; Kranz et al., 2016). Also, the void formation mechanism was widely studied and explained with Kirkendall effect by Urrejola (Urrejola et al., 2011). Further, another mechanism which is called surface energy minimization was suggested and a mathematical model was introduced for the quantitative description of void presence (Kranz et al., 2016). Dressler et al weakened the Urrejola’s claim by showing that heating time has the main influence on the void formation (Dressler et al., 2016). All of the theories are discussed individually in the section of “The Void Formation Mechanism” in Chapter 3.

CHAPTER 2

LASER PROCESS ON SILICON BASED SOLAR CELLS

2.1. Laser Applications in PV Industry

Lasers, which can be used as a source of heat and energy, has lots of application area in the PV industry. One of the laser-related processes is edge isolation in which emitter is removed from the edges to avoid shunting which leads to decrease in fill factor. As another example surface texturing, which is usually achieved by a wet chemical process in the industry, can be performed by laser. In this process, the shapes are formed on the surface by irradiating it with a laser beam to enhance light trapping properties and reduce the reflectance of the incident light. Ultrashort pulse lasers are more efficient for this process due to minimized damage on the Si surface.

Laser doping is another widely investigated process in which silicon surface coated with a material containing dopants were irradiated by laser to introduce the dopant atoms to the Si. Currently, this process is mostly applied to create selective emitter in which doping is locally performed.

Also, as mentioned before, a laser can be used for the contact processes. For instance, Si base deposited with a passivation layer and metal (evaporated or screen-printed) is locally irradiated by the laser, which melts the Al with the dielectric layer and Si to form Al-Si eutectic alloy through the passivation layer (Laser-Fired Contacts). Another example is the local contact opening (LCO) process that is widely discussed in the literature survey section for PERC type solar cells in which stack of layers on bulk material is locally ablated to collect photo-generated carriers by reducing recombination loss of metal-semiconductor interface. The LCO approach can be also applied to other types of solar cells such as heterojunction and interdigitated back contact (IBC) solar cells.

2.2. The Factors That Affect Laser Ablation Process

Basically, laser ablation is the removal of the material that is exposed to radiation. The absorbed laser beam breaks down the chemical bonds and solid material turns its phase to gaseous or plasma. The parameters known to affect the ablation process are: pulse duration, frequency, mark speed, beam quality, the material itself.

Wavelength

Absorption depth (x) can be expressed by Beer-Lambert law which is $I = I_0 e^{-\alpha x}$. Here, I is the transferred intensity where I_0 is the initial intensity and absorption coefficient (α) is dependent on the material and the incoming wavelength. For Si, the α values according to the wavelength and corresponding absorption depths according to wavelength are given in Figure 2.1. The wavelength should be selected according to desired absorption depth. For instance, IR wavelength is not widely used for the LCO process to avoid irradiating the bulk material.

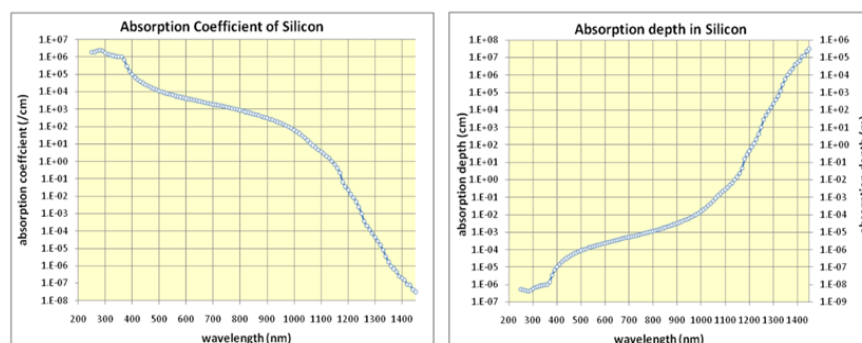


Figure 2.1. The absorption coefficient and corresponding absorption depth as a function of wavelength for Silicon material.

Pulse Repetition Rate (Pulse Repetition Frequency)

Pulse repetition rate can be defined as the number of emitted laser pulses in a second. The pulse repetition rate range can be varied according to the pulse generation technique. For instance, the range between 50 MHz and a few GHz can be obtained by mode-locked solid-state lasers. Also, cases such as smaller than 10 MHz and bigger than 100 GHz are possible. Moreover, gain switching semiconductor lasers can allow

pulse repetition rate from approximately 1 Hz to many MHz where this range is approximately between 1 Hz and order of 100 kHz for the Q switch solid-state lasers.

Pulse Duration (Pulse Width or Pulse Length)

Pulse duration can be defined as the full-width half maximum of the power vs time graph. However, the definition of the second moment of the temporal intensity profile can be more useful for the complicated pulse profiles. Further, in the laser-induced damage case, the effective pulse duration which is pulse energy divided by the peak power could be utilized.

The pulse duration can vary in a wide range. For instance, gain switching lasers can allow pulse duration from a few ns to some hundred ps. Another example is that Q-switched lasers can attain pulses with a duration between 100 ps and hundreds of ns. Moreover, pulse durations down to approximately 5 fs and up to hundreds of ps can be generated with mode-locked lasers.

During the propagation of the beam, pulse duration in the nanosecond or longer regime hardly varies but ultrashort pulses can be sensitive to chromatic dispersion, nonlinearities, optical filter. For the case of mode-locked lasers in the steady-state operation mode, pulse duration of the circulating pulses struggles with different effects, but it remains the same after every round trip.

Beam Quality

Beam quality can be explained as how well the beam can be focused at certain conditions. Sufficient beam quality, which can be obtained by the focusing skills, homogeneity, and brightness, is needed to have successful laser ablation. To quantify the laser beam quality, the beam parameter product (BPP) and M^2 factor can be used.

2.3. Theoretical Background of Laser Ablation

The energy given by the laser is absorbed by the free electrons and then transferred to lattice and ions. Additional energy is needed to form free carriers for the case of dielectrics and semiconductors, leading to the requirement of higher laser intensities.

For the free-electron case in low fluence, energy transfer can be expressed as follows;

$$C_e \frac{\partial T_e}{\partial t} = - \frac{\partial Q(z)}{\partial z} - \gamma(T_e - T_i) + S \quad (2.1)$$

$$C_i \frac{\partial T_i}{\partial t} = \gamma (T_e - T_i) \quad (2.2)$$

$$Q(z) = -k_e \frac{\partial T_e}{\partial z}, \quad S = I(t)A\alpha \exp(-\alpha z) \quad (2.3)$$

Here, T_e and T_i represent the temperature of the electron and lattice subsystem respectively where heat capacities are assigned by C_e and C_i . Heat flux is denoted by $Q(z)$ where z is the perpendicular direction to the surface and k_e is the thermal conductivity of electrons. Laser heating source term is denoted by S in terms of absorption coefficient α , laser intensity $I(t)$ and transmissivity $A=1-R$. Lastly, electron lattice coupling is characterized by γ parameter.

In this configuration, electron cooling time $\tau_e = C_e/\gamma$, lattice heating time $\tau_i = C_i / \gamma$ and pulse duration τ_L are significant time scales to determine nanosecond, picosecond and femtosecond regimes.

Femtosecond Regime ($\tau_L \ll \tau_e$)

In this case, the electron-lattice coupling time is comparable with τ_L . However, for some cases, it can be ignored since $C_e T_e / \tau_L \gg \gamma T_e$ to solve Eqn 2.1 easier. For further simplification, k_e can be ignored if the condition $D_e \tau_L < \alpha^{-2}$ is satisfied. D_e is the thermal diffusivity of the electron and equals to k_e/C_e . Moreover, C_e is equal to $C_e' T_e$ (C_e' is a constant) and $I(t)$ is accepted as constant I_0 . In light of this information, Eqn 2.1 can be reduced to:

$$C_e' \frac{\partial T_e^2}{\partial t} = 2 I_0 \alpha \exp(-\alpha z) \quad (2.4)$$

The solution of the differential equation 2.4 is:

$$T_e(t) = \left(T_0^2 + \frac{2I_a \alpha}{C_e'} t \exp(-\alpha z) \right)^{\frac{1}{2}} \quad (2.5)$$

In this equation $I_a = I_0 A$, and the initial temperature is denoted by T_0 . Hence the temperature of an electron after laser irradiation is as follows;

$$T_e(\tau_L) \sim \left(\frac{2F_a \alpha}{C_e'} \right)^{\frac{1}{2}} \exp\left(-\frac{z\alpha}{2}\right) \text{ where } F_a \text{ is absorbed fluence } (F_a = I_a \tau_L) \quad (2.6)$$

Since electron cooling is a very rapid process Eqn 2.2 can be written as follows by ignoring the initial lattice temperature:

$$T_i \sim T_e(\tau_L) t / \tau_i \quad (2.7)$$

If we put average cooling time $\tau_e^a = C_e' T_e(\tau_L) / 2\gamma$ to the formula 2.7, we get the following;

$$T_i \sim T_e^2(\tau_L) \frac{C_e'}{2C_i} \sim \frac{F_a \alpha}{C_i} \exp(-\alpha z) \quad (2.8)$$

From this equation F_a can be written as;

$$F_a \geq \frac{C_i T_i}{\alpha} \exp(\alpha z) \text{ where } \frac{C_i T_i}{\alpha} \sim F_{th} \quad (2.9)$$

F_{th} is the threshold fluence for strong evaporation in the femtosecond regime. If the expression is organized:

$$F_a \geq F_{th} \exp(\alpha z) \quad (2.10)$$

L (ablation depth per pulse) is equal to;

$$L \sim \alpha^{-1} \ln\left(\frac{F_a}{F_{th}}\right) \quad (2.11)$$

The logarithmic relation between ablation depth and fluence was experimentally shown many times (Byskov-Nielsen, 2010; Vladioiu et al., 2009; Yacob Ali et al., 2018)

Considering the time scale, a direct phase transition from solid to gasses or solid to plasma can be considered and thermal conduction into the bulk material can be neglected.

Picosecond Regime ($\tau_e \leq \tau_L \ll \tau_i$)

For a time scale $t \gg \tau_e$, the equation 2.1 can be reduced to;

$$\frac{\partial \left(k_e \left(\frac{\partial T_e}{\partial z} \right) \right)}{\partial z} - \gamma(T_e - T_i) + I_a \alpha \exp(-\alpha z) = 0 \quad (2.12)$$

And T_i can be written as;

$$T_i = \int_0^t \exp\left(-\frac{t-\theta}{\tau_i}\right) T_e(\theta) d\theta + T_0 \quad (2.13)$$

If $t \ll \tau_i$, this equation can be simplified to

$$T_i \sim T_e \left(1 - \exp\left(-\frac{t}{\tau_i}\right) \right) \sim \left(\frac{t}{\tau_i} \right) T_e \quad (2.14)$$

Based on this equation it can be said that lattice temperature remains much less than electron temperature in some cases. According to this, the T_i in Eqn 2.12 can be neglected. For the condition of $k_e T_e \alpha^2 \ll \gamma T_e$, the temperature of electron and lattice after laser irritation can be expressed as follows:

$$T_e \sim \frac{I_a \alpha}{\gamma} \exp(-\alpha z), \quad T_i \sim \frac{F_a \alpha}{C_i} \exp(-\alpha z) \quad (2.15)$$

As it is seen, the expression of lattice temperature is the same for both femtosecond and picosecond regime. Thus the strong evaporation condition coming from Eqn 2.10 and logarithmic relation between ablation depth and fluence shown in Eqn 2.11 remains the same.

Heat conduction into the material is neglected during the derivations, which is a crude assumption considering the picosecond regime. Still, a direct transition from solid to gasses or solid to plasma is valid.

Nanosecond Regime ($\tau_i \ll \tau_L$)

Nanosecond regime will be mentioned very briefly. Temperatures of the electron and lattice are equal to each other, and indicated by T. So, the Eqn 2.1 can be expressed as:

$$C_i \frac{\partial T}{\partial t} = \frac{\partial (k_0 \frac{\partial T}{\partial z})}{\partial z} + I_a \alpha \exp(-\alpha z) \quad (2.16)$$

For long laser pulse cases, there is enough time for heat conduction and to form melted material, and evaporation arises from the liquid material. As a consequence of this, thermal damage on the surface is higher compared to other regimes.

CHAPTER 3

REAR CONTACT FORMATION IN PERC TYPE SOLAR CELLS

3.1. Contact Formation Mechanism

Inter diffusion of Al and Si through LCOs of a PERC type c-Si solar cells creates rear contacts during the firing process, where the BSF layer is the consequence of the highly Al-doped epitaxially grown excess Si at the Si (solid) / Si-Al (liquid) interface.

The Al-Si phase diagram in Figure 3.1 shows the thermodynamic behaviors at equilibrium. The diffusion process between Al and Si is explained by this diagram.

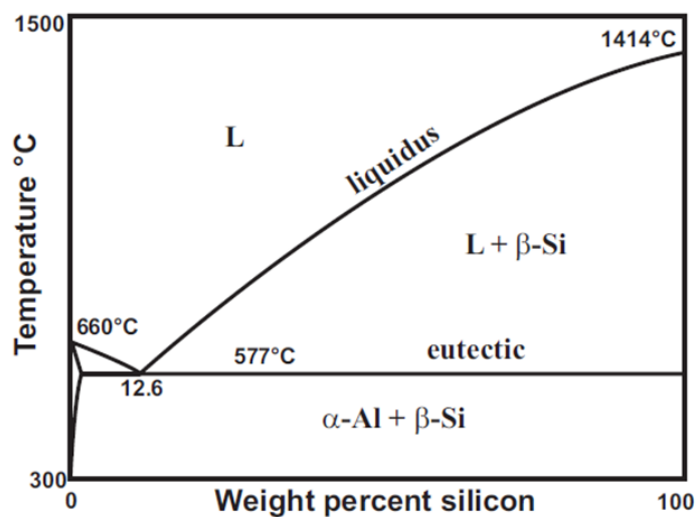


Figure 3.1. Al-Si phase diagram

However fast heating and cooling times during the firing process may cause deterioration in equilibrium. It is assumed that thermodynamic conditions of equilibrium are satisfied during the firing process. The interaction between Si and Al for both homogenous case and LCO case occur as follows and is shown in Figure 3.2;

- 1- Solid silicon starts to dissolve in solid Al matrix at ~ 300 °C and the solid solubility increases with temperature (it is maximum at eutectic temperature 577 °C).
- 2- Al changes its phase from solid to liquid at a melting temperature ~ 660 °C. On the other hand, the melting point of Si is 1414 °C. Hence, Si is dissolved by the Al melt and forms Al-Si melt at the interface. The melt penetrates the bulk. As a side note, the oxide layer around the Al particles conserves the form of the Al matrix during the alloying process.
- 3- The concentration of the Si in the melt can be determined according to temperature. The liquid line in Figure 3.1 shows the Si concentration raise with increased temperature. Usually, the peak firing temperature is around 850 °C in the PERC industry, which corresponds to 30% Si concentration in the melt at equilibrium. At this point, there is a difference between standard solar cells and PERC solar cells. The inter diffusion occurs through the LCOs for PERC and hence Si saturation in the Al matrix appears faster near the interface of Si-Al and forms Gaussian profile for the Si concentration that is shown in Figure 3.2.
- 4- During the cooling, Si concentration reduces as the temperature decreases (see the liquid line in Figure 3.1 again). As a consequence of this, the extracted Si grows epitaxially at the solid-liquid interface, which forms the p+ layer. Another mechanism that contributes the BSF is solid solubility of Al into Si. For the LCO case, the Si has driven away from the openings. Hence Al-doped Si concentration near the contacts may not be enough for recrystallization to create BSF during the cooling down, leading to shallow BSF with low doping or no BSF. As an extreme case, available Si concentration that is below the eutectic concentration at the beginning of the cooling down step cause non-existed BSF. This situation may occur when the LCOs are too narrow and accordingly low concentration of Si is available for dissolution or Si has driven away too far from the contact in the Al paste.
- 5- Lastly, the whole liquid turns into solid under the eutectic temperature.

The resulted contacts in this configuration, can be assigned with one of the three categories which are filled contact, partial void, void as shown in Figure 1.12.

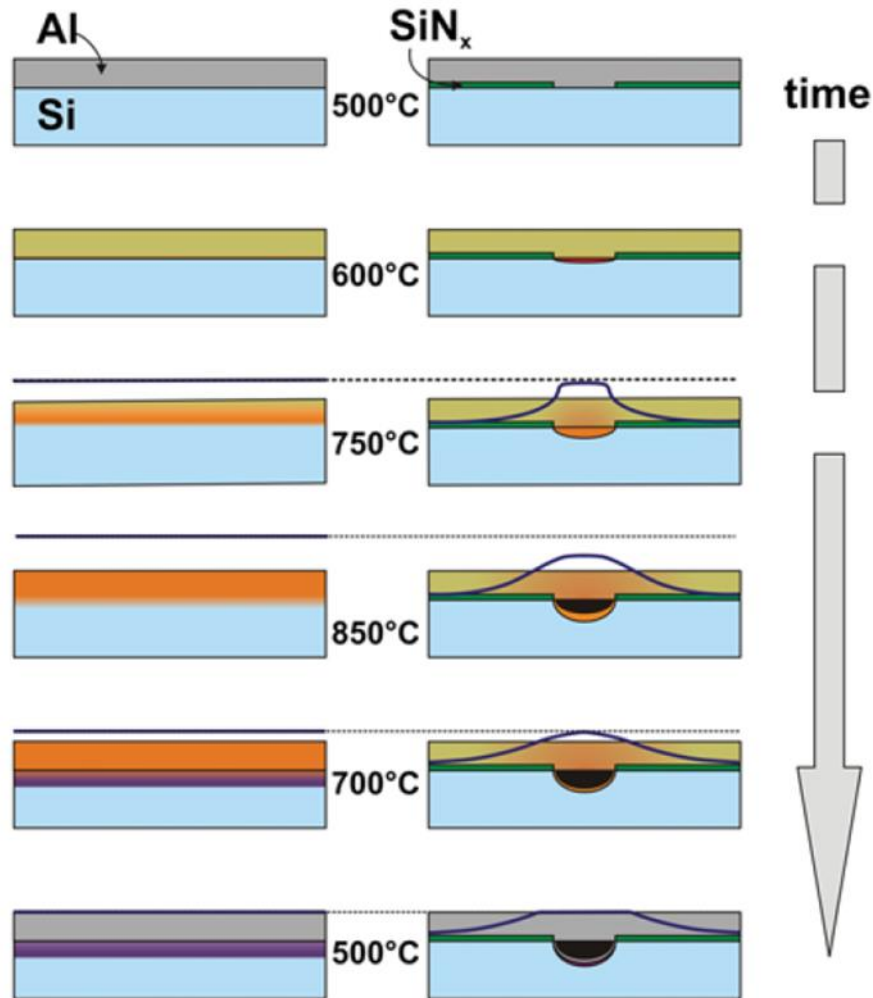


Figure 3.2. Illustration of the rear contact formation for the homogenous and LCO case. Si concentration in the Al paste is represented by the curve while Si solubility according to temperature is represented by the dash line. (Lauer mann et al., 2015)

3.2. Void Formation Mechanisms

There are different theories related to the void formation mechanism. Urrejola explains it by Kirkendall effect (Urrejola et al., 2011). Based on this explanation, the diffusivity velocity difference between the materials causes void formation. To be more specific, Si and Al diffuse in each other however Si diffusion in the Al matrix is

faster than Al diffusion in Si, which results in voids at the interface during the melting of the firing process. Then, Si is driven away from LCOs due to strong lateral concentration gradient and may not be able to travel back during the fast cooling down of the firing process. This leads to void contacts (Figure 1.12c). Further, another mechanism which is called surface energy minimization was suggested (Kranz et al., 2016). According to this approach, the presence of voids with BSFs is proof that void formation occurs toward the end of the firing process. Also, it is observed that voids have shallower BSF depth compared to filled contacts in general, leading to the argument that epitaxial BSF growth stops once the Al-Si melt loses contact with the Si bulk. Based on these estimations, the model proposes that during cooling down, the surface tension of the Al-Si melt prevents the adhesion of the melt to the exposed Si surface. This may tear off the melt from the surface. Also, an analytical model was suggested by using minimizing of the surface energies of the silicon wafer surface, the liquid Al, and the screen-printed Al particle surface for the quantitative description of void presence (Kranz et al., 2016).

3.3. The Mathematical Models for the Al:BSF Depth

Muller suggested a mathematical model for the quantitative description of Al:BSF depth. Later, Laurmann extended the model by involving differential equations that define the Gaussian profile of Si concentration in the Al matrix.

The BSF depth strongly depends on the Si concentration of Al paste, size, and shape of the LCO, the distance between the contacts as well as the firing profile and opening technique. The studies related to these issues are presented in the Literature Survey part in Chapter 1. An explanation was offered by Müller with an analytical model that gives the BSF depth as a function of firing profile and contact geometry.

The concentration of Si in the Al-Si liquid (c_{Si}) was given as follows;

$$c_{Si}(t) = \frac{m_{Si}}{m_{Si} + m_{Al}} \quad (3.1)$$

m_{Si} and m_{Al} stand for the mass of the Si and Al which helps to form an alloy respectively. c_{Si} depends on time and it is assumed that its lateral distribution is homogenous over time for simplicity. Essentially, it is not homogenous and has a Gaussian profile as it is shown in Figure 3.2.

When the eutectic composition ($E \sim 12\%$) was reached, Si stops to segregate and the liquid solidifies. So, the mass of the recrystallized Si can be written as:

$$m_{Si,BSF} = m_{Al} \left[\frac{c_{Si}(t_{firing})}{1 - c_{Si}(t_{firing})} - \frac{E}{1 - E} \right] \quad (3.2)$$

So, the depth of the Al:BSF can be shown as follows:

$$W_{BSF} = \frac{m_{Al}}{A\rho_{Si}} \left[\frac{c_{Si}(t_{firing})}{1 - c_{Si}(t_{firing})} - \frac{E}{1 - E} \right] \quad (3.3)$$

Here, the density of Si in Al:BSF was denoted by ρ_{Si} . Cuboidal shape contact as shown in Figure 3.3 was assumed and the area of the contact after firing was represented by A.

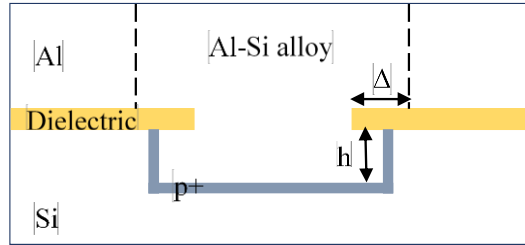


Figure 3.3. Illustration of assumed contact geometry that shows h and Δ values

In the LCO case, the dielectric layer act as a barrier and only a part of the Al paste contributes to sintering. The contributing Al on the one side of the contact was denoted by Δ (see Figure 3.3).

For the line contact case the mass of the Al that contributes alloy formation can be written as:

$$m_{Al} = d(a + 2\Delta)p\rho_{Al} \quad (3.4)$$

On the other hand, m_{Al} can be determined as follow for the point contacts;

$$m_{Al} = d\pi (r + \Delta)^2 \rho_{Al} \quad (3.5)$$

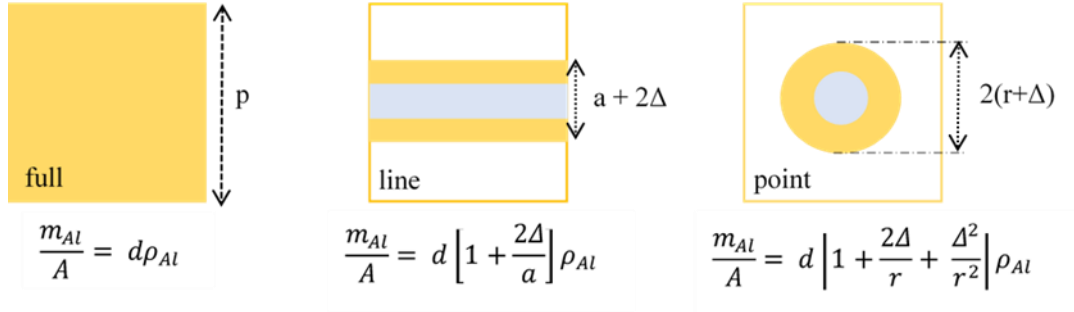


Figure 3.4. The ratio of m_{Al} / A for different contact geometries: full area, line, point. Here, contact width after firing is denoted by a .

The ration of m_{Al}/A strongly depends on the shape of the contacts as shown in Figure 3.4. d is the thickness of the Al paste; p is the distance between the contacts (pitch) and ρ_{Al} stands for the Al density.

Moreover, it should be considered that the firing process takes place in a short time which does not let to reach equilibrium conditions. However, it is assumed that T_{firing} (firing temperature) controls the F (the equilibrium Si concentration) is constant. Hence, the Si concentration over time can be defined as follow:

$$\frac{dc_{Si}(t)}{dt} = k [F - c_{Si}(t)] \quad (3.6) \text{ where } k \text{ is a constant}$$

The solution for this equation is:

$$c_{Si}(t) = F (1 - e^{-kt}) \quad (3.7)$$

By applying the boundary condition of $c_{Si}(t) = 0$ at $t=0$ we can get:

$$\frac{dc_{Si}}{dt} \sim \frac{1}{m_{Al}} \frac{dm_{Si}}{dt} = \frac{A\rho_{Si}}{m_{Al}} \frac{dh}{dt} \quad (3.8)$$

h is the contact depth as shown in Figure 3.3. By combining Eqn 3.6 and 3.8 we can write the k value as:

$$k = \frac{A}{m_{Al}} \frac{\rho_{Si} v_{diss}}{F} \quad (3.9) \text{ where } v_{diss} (\text{dissolution velocity of Si}) = \frac{dh}{dt}$$

Correspondingly, W_{BSF} equals to:

$$W_{BSF} = \frac{m_{Al}}{A\rho_{Si}} \left[\frac{F \left(1 - e^{\frac{-A\rho_{Si}V_{diss}}{m_{Al}F} t_{firing}} \right)}{1 - F \left(1 - e^{\frac{-A\rho_{Si}V_{diss}}{m_{Al}F} t_{firing}} \right)} - \frac{E}{1 - E} \right] \quad (3.10)$$

The other model that is suggested predicts the BSF depth with a doping profile, which is useful to determine effective rear side recombination velocity and input parameters for simulations (Lauermaun, 2016). The difference of this model from Muller's model is that it roughly follows the Gaussian profile for the Si redistribution movement in the Al matrix and analysis the Si concentration above the contacts.

Again we start with the definition of Si concentration in the molten Al paste however this time it is a function of time t and position x .

$$C_{Si}(t, x) = \frac{m_{Si,diss}(t, x)}{m_{Al} + m_{Si,diss}(t, x)} \quad (3.11)$$

The first assumption is that the total Al is constant in terms of time and homogenously distributed. This is accurate because approximately 0.01% of the Al which is negligible incorporates to BSF. Secondly, LCO depth was not considered due to its small influences.

It is useful to remember that diffusivity is a strong function of temperature and hence the peak firing temperature has significant impact on diffusion process.

For the simplicity reasons, the problem was divided into three-part that is given below and demonstrated in Figure 3.5;

- I. The heating up process in which the local saturation of the Al paste is present until the peak firing temperature T_{peak} .
- II. The diffusion process at the T_{peak} .

III. The cooling down process in which epitaxially Al:BSF growth takes place.

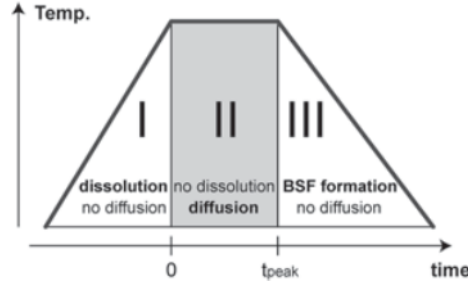


Figure 3.5. Simplified firing model according to time

At the end of Part I, it is assumed that the total width of the lateral distribution of the Si in the Al matrix is $2w$ ($-w \leq x \leq w$). When $t=0$ (the beginning of part II) $c_{Si}(0,x)$ can be expressed in terms of Heaviside step functions as follows:

$$c_{Si}(0, x) = c_0(T_{peak}) * [\theta(x + w) - \theta(x - w)] \quad (3.12)$$

The differential equation below should be solved for the c_{Si} by assuming that Si concentration in the paste is homogenous throughout the height of the Al matrix (there is only lateral variation).

$$\frac{\partial}{\partial x} c_{Si}(t, x) = \frac{\partial^2}{\partial x^2} c_{Si}(t, x) \quad (3.13)$$

There is a fundamental solution for Eqn 3.13:

$$G(t, x) = \frac{1}{\sqrt{4\pi Dt}} * \exp\left(-\frac{x^2}{4Dt}\right) \quad (3.14)$$

This is an obvious Gaussian distribution and it is used as a Green's function to generate a solution to Eqn 3.12 (the initial condition).

$$c_{Si} = \int_{-\infty}^{\infty} G(t, x - y) * c(0, y) dy = \frac{c_0(T_{peak})}{\sqrt{4\pi Dt}} \int_{-\infty}^{\infty} \exp\left(-\frac{(x - y)^2}{4Dt}\right) * [\theta(y + x) - \theta(y - x)] dy$$

It is known that the integration of the Heaviside step function gives sum of error functions. Hence, at the end of part II, silicon concentration in the Al matrix as a function of time and position is as follows:

$$c_{Si}(t, x) = \frac{1}{2} c_0(T_{peak}) * [erf\left(\frac{x+w}{\sqrt{4Dt}}\right) - erf\left(\frac{x-w}{\sqrt{4Dt}}\right)] \quad (3.15)$$

It meets the mass conservation law, since the following equation hold for every t.

$$\int_{-\infty}^{\infty} [erf\left(\frac{x+w}{\sqrt{4Dt}}\right) - erf\left(\frac{x-w}{\sqrt{4Dt}}\right)] dx = 4w \quad (3.16)$$

The max Al:BSF depth can be expressed as follows for the alloy of height h:

$$d_{BSF} = \frac{\rho_{alloy}}{\rho_{Si}} * \left(\frac{C_{Si}(t_{peak}, 0)}{1 - C_{Si}(t_{peak}, 0)} - \frac{C_{eut}}{1 - C_{eut}} \right) * h \quad (3.17)$$

CHAPTER 4

DEVICE FABRICATION

This chapter is organized into two parts. In the first part, the effects of the distance between the Local Surface Openings (LCOs) on solar cell performance are presented while in the second part the effects of the different laser parameters on LCOs, rear contact formation and solar cell performance are discussed.

For both studies, 1-3 $\Omega\cdot\text{cm}$, CZ grown, 180 μm thick, p-type mono c-Si wafers were used in fabrication and characterization. After the texturing and cleaning of these wafers, the doping process was performed. To provide electrical isolation, the rear side was etched (single side etching) to remove the Si layer with a thickness of around 10 μm . The front surface was coated with SiN_x that serves as the antireflection coating and passivation layer while the rear surface was coated with SiN_xO_y for back surface passivation and SiN_x as a capping layer. For both SiN_xO_y and SiN_x deposition plasma enhanced chemical vapor deposition (PECVD) technique was used. Then the laser ablation process was performed to create LCOs before the metallization and firing steps. By keeping other process steps identical, the laser ablation process was performed in different ways. This simple process sequence is shown in Figure 4.1 and the details of the processes are given in the following sections.

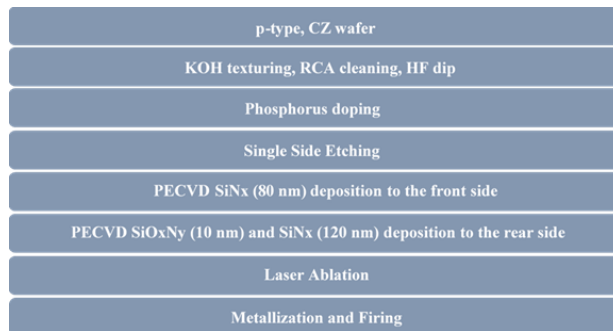


Figure 4.1. Simplified process sequence of the experiments

4.1. Fabrication Procedure for the Study “Effects of the Pitch on Solar Cell Performance”

In this study, the effects of the distance between the LCOs on solar cell performance were investigated. The design of the experiment is shown in the laser ablation section. Also, other necessary steps for device fabrication are explained in detail below.

4.1.1. Wet Chemical Steps: Texturing and Cleaning

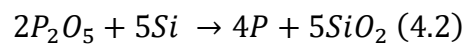
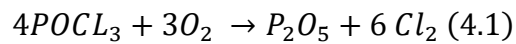
Rena BatchTex is used for the texturing and cleaning steps. Random pyramids were formed on the surfaces in the potassium hydroxide (KOH) and Mono-TEX (a non-flammable moderating and wetting agent developed by RENA) solution, enabling reduction in the reflection of light from the surface and consequently increment of the photon coupling in the Si base. Radio Corporation of America (RCA)1 and RCA2 cleaning steps were performed to remove organic and metallic contaminants respectively. The RCA1 solution consists of H₂O: NH₄OH (ammonium hydroxide): H₂O₂ (hydrogen peroxide) with the ratio of 6:1:1 while RCA2 solution consists of H₂O:HCl (hydrochloric acid):H₂O₂ with the ratio of 6:1:1 .

Also, native oxide layers on the surfaces were removed when necessary, for instance immediately before the PECVD process, in %5 diluted HF solution until the surface becomes hydrophobic due to the termination of hydrogen.

4.1.2. Doping

After texturing and cleaning steps, p-type wafers were subjected to phosphorous diffusion to create p-n junction. Phosphorous atoms are n-type dopants for Si and there are some considerations related to the doping level. The lowly doped n-type layer should be created to decrease Auger recombination which leads to a reduction in Voc. On the other hand, high doping is required for the better lateral transport of the generated carriers and hence low resistance. Thus, a balance between these considerations should be achieved.

After the HF immersion and drying, the wafers were placed into the diffusion furnace with the brand name Don Guan. Phosphorus oxychloride (POCl₃) and oxygen (O₂) were used as a source where nitrogen (N₂) was a carrier gas. The procedure mainly consists of two parts which are pre-deposition and drive-in. Firstly, dopants were introduced to the substrate in the glass form (pre-deposition) and then drive-in anneal was performed for the diffusion of the atoms from glass to the substrate. The simplified reactions are given below:



As can be seen from Eqn 4.2, a phosphosilicate glass layer is formed on the surface after the process and it was removed during the Single side etching process.

4.1.3. Single Side Etching (SSE)

To provide electrical isolation SSE was performed in an inline RENA system. In the first batch of this device, the PSG layer on the rear side was removed with diluted HF by protecting the front PSG layer with water. Then, the rear side was subjected to H₂SO₄ and HNO₃ solution for the etching process while keeping the front side unexposed. After rinsing of both side, diluted KOH was applied to reduce the surface roughness. Then, both sides were subjected to HF/HCl acidic batch for cleaning after the second rinse. Lastly, drying was performed after the last rinse. As a consequence of this process, the rear side of the wafers was etched 10 μm from the surface.

4.1.4. Plasma Enhanced Chemical Vapor Deposition (PECVD)

The deposition of SiN_x for the front and rear side, and SiO_xN_y for the rear side was performed with a pilot size tube type low frequency (50 Hz) PECVD tool with the brand name Don Guan. For the process, wafers were placed in between graphite plates directed face to face and plasma were created in between two wafers as shown in Figure 4.2.

At the front side, ~80 nm of the PECVD SiN_x layer was used for its anti-reflection properties as well as field-effect passivation and bulk hydrogenation properties. The important aspects that should be taken into consideration about this layer are optimum refractive index and thickness to attain minimum reflection, and homogeneity to prevent mismatch losses on module level. As a precursor SiH₄ and NH₃ were used where N₂ as a carrier gas and the reaction for the layer formation can be simplified as follows:

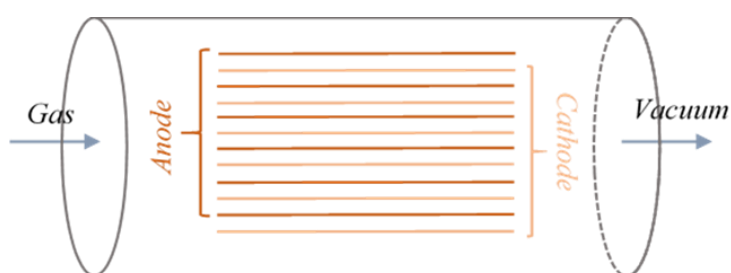
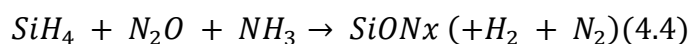


Figure 4.2. Illustration of the PECVD system from top view

SiO_xN_y (~ 10 nm) was coated on the rear surface of the wafer as a passivation layer immediately before SiN_x (~120 nm) deposition as a capping layer. The same procedure was followed for the SiN_x deposition with different process time. On the other hand, SiH₄, NH₃, and N₂O was used as a precursor for the SiO_xN_y deposition process and the reaction is given in Eqn 4.4;



4.1.5. Laser Ablation

Laser ablation, the main subject of this thesis, was performed by the Innolas Picosecond Laser System which is explained in section 4.2.1.1 explicitly.

In this study, the effects of the distance between the LCOs were investigated. LCOs that have 30-55-105 μm width were opened with the pitch of 0.5, 1, 1.5, 2, 3 mm. To decrease the effects of local variations in the wafer, the same parameters were applied to 3 wafers in a way that coincides with a different location. The designs of these

wafers are presented on the PL images taken after the laser ablation process in Figure 4.3.

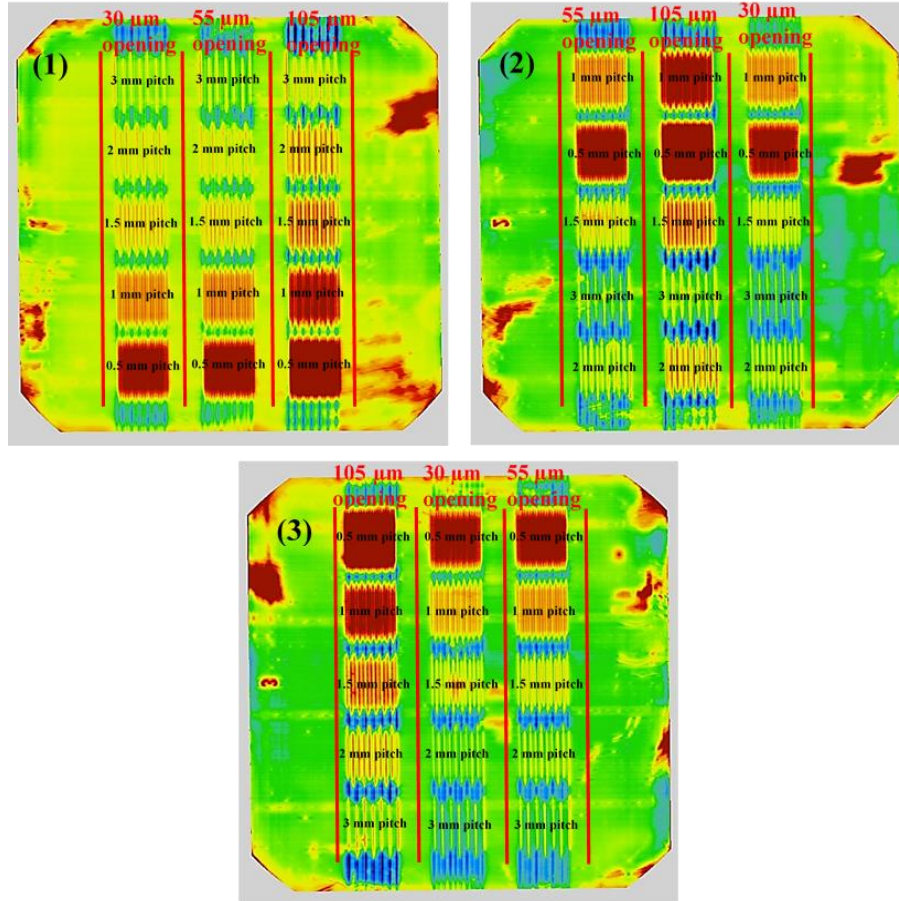


Figure 4.3. The laser ablation design of the experiment

4.1.6. Metallization and Firing

Screen printing metallization of rear side aluminum (Al) and front side silver, and firing process in a belt furnace were performed to form contacts. As mentioned before rear contact formation is affected by Al paste composition and thickness, firing profile. Hence, the details of them are critical and given in the following sections.

Al Paste

For industrial PERC applications, screen printing of Al paste process is the most preferred one since it is cheap, high-throughput process and its technology has been

already proven for full-area Al-BSF solar cells without rear passivation. TOYO Al paste was screen printed with thickness 30 μm and its integrands are given in the following table.

Table 4.1. *Ingredients of the Al paste*

Ingredients	<i>M</i>
Aluminum	70-85
Lead free glass	≤ 5
Resin	≤ 5
Solvent	Residue

Firing Profile

We have used SINTER firing belt furnace consist of 6 zones which can be arranged. The temperature of zone 6 (last zone) is the peak one, and then the sample starts to cool down until it comes out. Another variable for the furnace is belt speed which can move with a speed up to 500 cm/s. Since the previous studies conducted in GÜNAM showed that 930 $^{\circ}\text{C}$ peak firing temperature and 500 cm/s belt speed were best for the front contacts to achieve higher solar cell performances, the temperature of the first 5 zones were varied based on the study (Dressler et al., 2016) and (D. Chen et al., 2013) that aims void reduction. Although lower peak firing temperature is needed to reduce void formation, high peak temperature has to be applied for silver front contacts. Hence, the peak temperature was kept constant at 930 $^{\circ}\text{C}$ while other parameters were varied to achieve the best heating time. A reference firing profile was generated based on standard firing profile used in the industry which includes a small plateau at 550 $^{\circ}\text{C}$ and peak wafer temperature at 800 $^{\circ}\text{C}$. The time that is passed for heating (550 $^{\circ}\text{C}$ to 800 $^{\circ}\text{C}$) and cooling (800 $^{\circ}\text{C}$ to eutectic temperature 577 $^{\circ}\text{C}$) is approximately 5 seconds. 5 different firing profiles given in Table 4.2 (including the reference firing profile that is labeled with number 1) were applied to 25 identical samples (5 samples for each firing profile). Heating time and accordingly interaction time between liquid Al - solid Si, thermal budget increases from 1 to 5. An important note here is that the

temperature we specify in the computer program (given in Table 4.2) is not the same as the thermocouple measurements. For instance, 930 °C on the program, which is the highest allowed temperature, corresponds to ~790 °C in the furnace according to thermocouple measurements.

One obvious result was that BSF gets deeper up to 12 μm as the thermal budget increases. However, photovoltaic results were not affected in a good way with increasing thermal budget. Considering these results that are presented in the Results and Discussions chapter, we decided to apply the standard firing profile in this thesis work.

Table 4.2. *Applied firing profiles*

Firing Profile	Temperature (°C)					
	Zone 1	Zone 2	Zone 3	Zone 4	Zone 5	Zone 6
1 (reference)	300	450	500	650	800	930
2	300	450	850	850	850	930
3	300	650	850	850	850	930
4	300	750	850	850	850	930
5	450	750	850	850	850	930

After these processes, the I-V results of the prepared solar cells were investigated with the help of a solar simulator and the results of them are presented in the Results and Discussions part.

4.2. Fabrication Procedure for the Study “Effects of Laser Parameters on Contact Formation and Solar Cell Performance”

In this experiment, the device fabrication process sequence was the same as the previous study “Effects of the pitch on solar cell performance”. The only difference in this case is the laser ablation process that was performed differently as described in the following section.

4.2.1. Laser Ablation and Characterization Process

The LCO process was performed with different laser parameters such as frequency, power by keeping the pitch constant at 1 mm, 1.5 mm, 2 mm. To have the accuracy, the corresponding laser fluence for each parameter was calculated from maximum average laser power P_{avg} and respectively pulse energy E_p as in following equations 4.5 and 4.6, where beam radius is denoted by r and hence beam spot area by πr^2 . Beam radius can be defined as the distance from the beam axis where the intensity drops to $1/e$ of its peak and it is equal to $37.5 \mu\text{m}$ for our system.

$$E_p = \frac{P_{avg}}{\text{Repitition frequency } (f_{rep})} \quad (4.5)$$

$$\text{Pulse Fluence} \left(\frac{\text{Joule}}{\text{cm}^2} \right) = \frac{2E_p}{\pi r^2} \quad (4.6)$$

First, the ablated area on the stack of SiO_xN_y and SiN_x , was analyzed by visual inspection through optical microscopy and SEM. Then, contact characteristics detected by SEM imaging such as void ratio, BSF thickness, and contact width were analyzed as a function of laser fluence. Further, the effects of contact characteristics on cell performance were discussed according to efficiency results. For this purpose, solar cells with the size of $2 \times 2 \text{ cm}^2$ were prepared from full-size wafers (15 solar cells from a full wafer). Further, corresponding efficiencies were calculated for each fluence by using 2D device simulation Quokka with input parameters given in Table 5.3. As a result, an optimum fluence range was determined for PERC production. Lastly, 60 solar cells were produced with a size of 121 cm^2 by applying the chosen fluence.

4.2.1.1. Innolas Picosecond Laser System used in the Studies

The laser system (Figure 4.4a) is designed for the 156-156 mm or 125-125 mm wafers used in the PV industry and run by CNC (Computer Numerical Control) and PLC (Programmable Logic Controller). In Figure 4.4b, the relation between individual control assemblies can be seen.

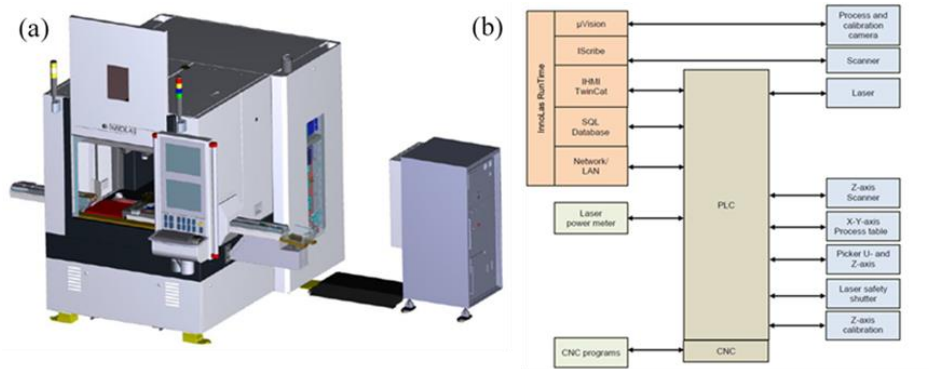


Figure 4.4. (a) Illustration of the Innolas Picosecond Laser System and (b) scheme that shows the relation between assemblies

Coherent Hyper Rapid 25 HE laser is used in the system. It is a diode-pumped mode-locked laser that emits short pulses (7-10 ps) in IR wavelength range with high pulse energy. Also, the wavelength can be tuned to 532 nm which is in the green region (second harmonic). Moreover, the repetition rate frequency (RPF) can be varied from 200 kHz to 1 MHz.

Constant pulse trains within 50 MHz RPF are generated by the seeder laser in the laser head. Then the electro-optical modulator (EOM), which is also called pulse picker, chooses single pulses from the pulse train. While the unused pulses deviate through the beam dump, the selected ones will be amplified to reach the required energy. This simplified sequence is shown in Figure 4.5.

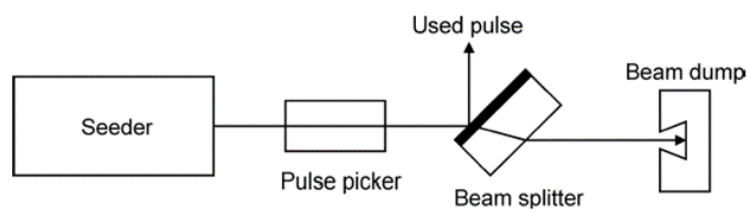


Figure 4.5. Principle function of EOM

Fast high voltage is applied to the EOM synchronously to the seeder pulse train to change the polarization of a signal pulse. p polarized pulse turns into s polarized or vice versa (Figure 4.6).

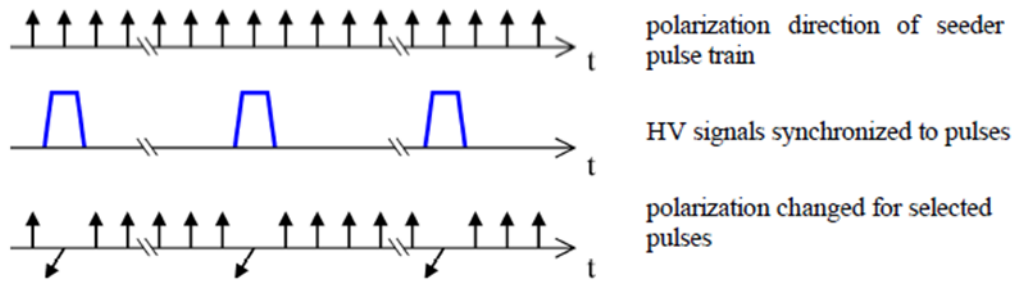


Figure 4.6. Illustration that shows the correlation between the polarization and fast high voltage signal

More specifically, the reaction time of the EOM is approximately 5 ns which is smaller than the time between pulses (20 ns). This process is illustrated in the following Figure 4.7. Then polarization filters lead to signals to their paths. Hence, we can select certain laser pulses and amplify them.

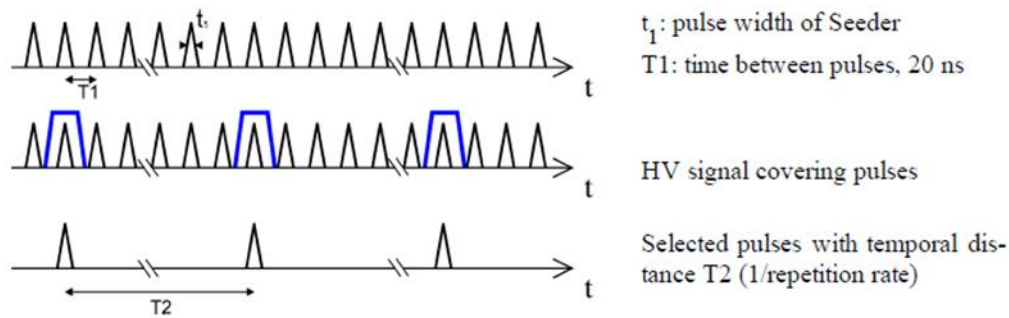


Figure 4.7. Correlation between high voltage signal and pulses

Moreover, the second harmonic generation is achieved in a nonlinear optical crystal. The frequency conversion module that contains these optical elements is added to the front of the laser head. The schematic design of the laser system can be examined in Figure 4.8. Only, we don't have THG crystal that is shown in Figure 4.8 in our system.

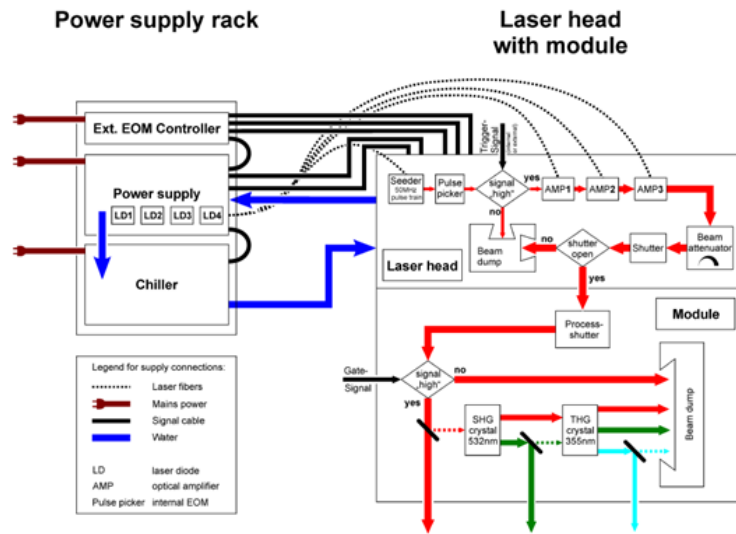


Figure 4.8. Schematic design of the laser system

Laser Parameters Used in the Studies

Second Harmonic mode (532 nm) at frequencies from 200 kHz to 1MHz, is used for this thesis. For each parameter, laser power is determined by using the in-built power meter. Figure 4.9 represents the power variations depend on frequency and attenuator. Power decreases with increasing frequency. On the other hand, the attenuator is controlled by the program and decreases the laser power in a non-linear way by changing the motor position. The max average power used in the study was 18.4 W. The laser beam scanner has a maximum scan speed of 20 m/s. The applied laser parameters are summarized in Table 4.3.

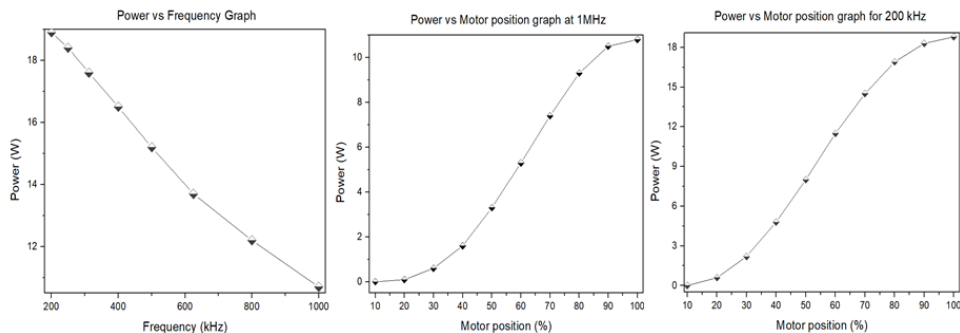


Figure 4.9. Measured power values according to frequency (a) and motor positions when 1 MHz frequency was used (b) and 200 kHz frequency was used (c)

Table 4.3. *Applied Laser Parameters*

Parameter	Value
Wavelength λ (nm)	532
Pulse Duration (ps)	10
Repetition rate (kHz)	200-1000
Beam diameter (μm)	75
Max average laser power P_{avg} (W)	18.4 at 200 kHz
Max pulse energy E_p (μJ)	92 at 200 kHz
Max peak fluence F_p (J/cm^2)	4.2 at 200 kHz
Scan speed	15 m/s

CHAPTER 5

RESULTS AND DISCUSSIONS

In the first part of the thesis, the influence of the heating time of the firing process on BSF formation and solar cell performance was examined. Then, the effects of the distance between the contacts on solar cell performance were investigated to decide the contact pitch for further studies. Moreover, ablated regions on the dielectric layers were analyzed and the relation between the fluence and LCO width was discussed. Also, the effects of the different laser parameters on contact behaviors such as contact width, BSF depth, void formation, and solar cell performance were investigated, and then the effects of the contact behaviors on solar cell performance were discussed. Further, corresponding efficiencies were calculated for each fluence by Quokka simulation. According to these results, an optimized fluence range was determined for PERC solar cell fabrication.

5.1. The Effects of Firing Profiles on BSF Formation and Solar Cell Performance

Before starting the major experimental study, we conducted a series of experiments to determine firing recipe as a controlled parameter. Five different recipes that have different heating time were applied to 5 samples for each. It is observed that BSF get deeper up to 12 μm as the heating time increases. This can be examined in the SEM images presented in the Figure 5.1.

However, when effects of the different firing profiles on the solar cell performance was examined, it is observed that efficiency tends to decrease as the heating time increases and thermal budget increases with the heating time. The I-V results of the prepared 25 cells are presented in the Fig. 5.2.

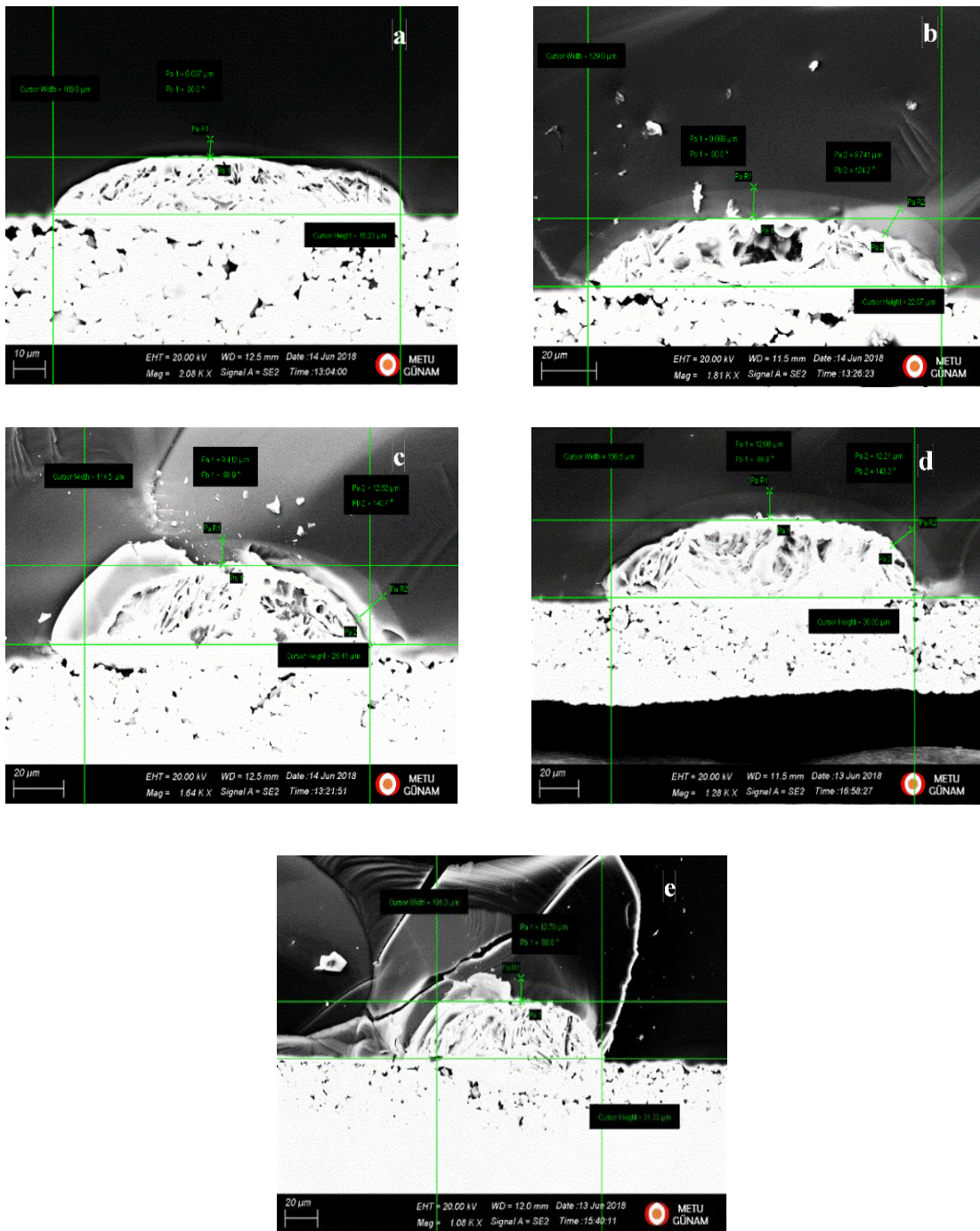


Figure 5.1. SEM images of the rear contacts that shows BSF depths for the firing profiles which are (a) standard (b) 300-450-850-850-850-930 (c) 300-650-850-850-850-930 (d) 300-750-850-850-850-930 (e) 450-750-850-850-850-930 were applied.

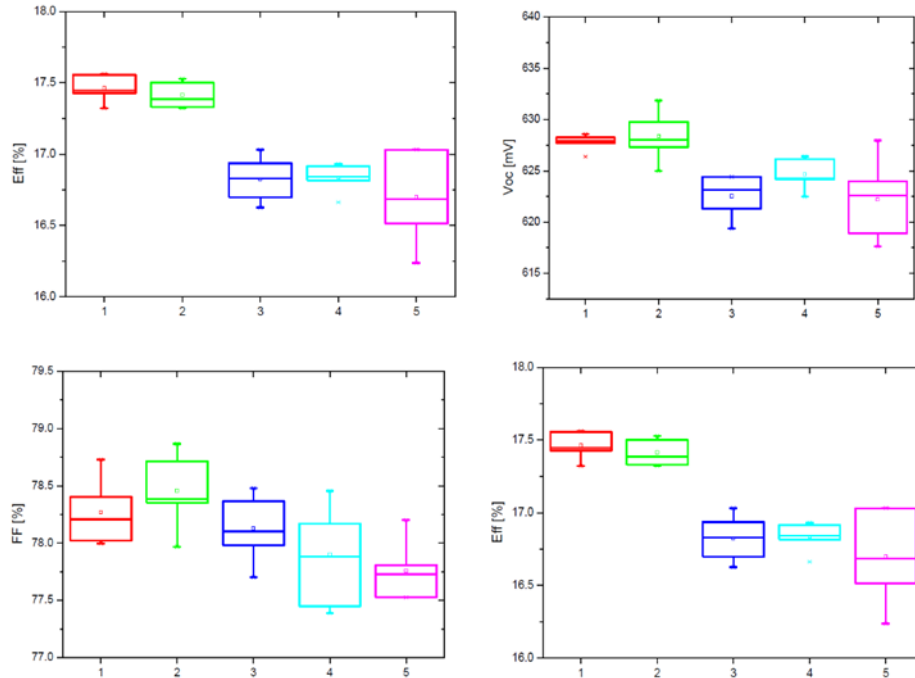


Figure 5.2. I-V results of the 25 samples

The possible reason for the general decrease in efficiency could be the front finger width increment with thermal budget increment. An example of this situation is shown in Figure 5.3a on SEM images. 10 front fingers were measured for each solar cell and their average was calculated as given in Figure 5.3b.

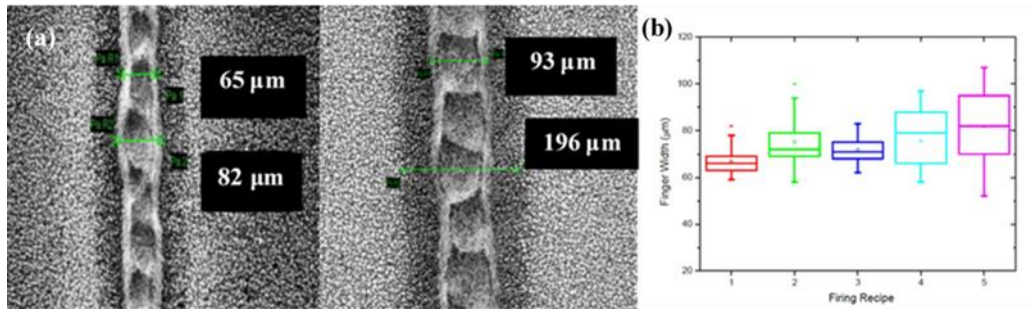


Figure 5.3. (a) SEM images of the front fingers (b) average of the front finger widths for each wafer. Considering these I-V results, the thermal budget and the study (S. Gatz et al., 2012) showing that surface recombination velocity is constant after a minimum of 4 μm BSF depth is reached (Figure 5.4), reference firing profile is applied as a controlled parameter.

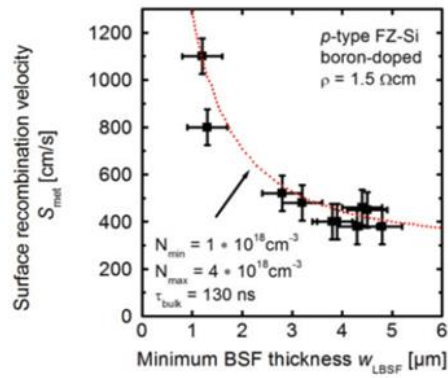


Figure 5.4. Calculated surface recombination velocity values according to with min BSF thickness from study (S. Gatz et al., 2012).

5.2. The Effects of the Pitch on Solar Cell Parameters

In Figure 5.5, the solar cell parameters of this study are represented. In here 50,70 μ m represents the rear contact width after firing while the x-axis shows the distance between the rear contacts. Hence, the metallization fraction decreases as the rear contact width decreases and towards to the right on the x-axis.

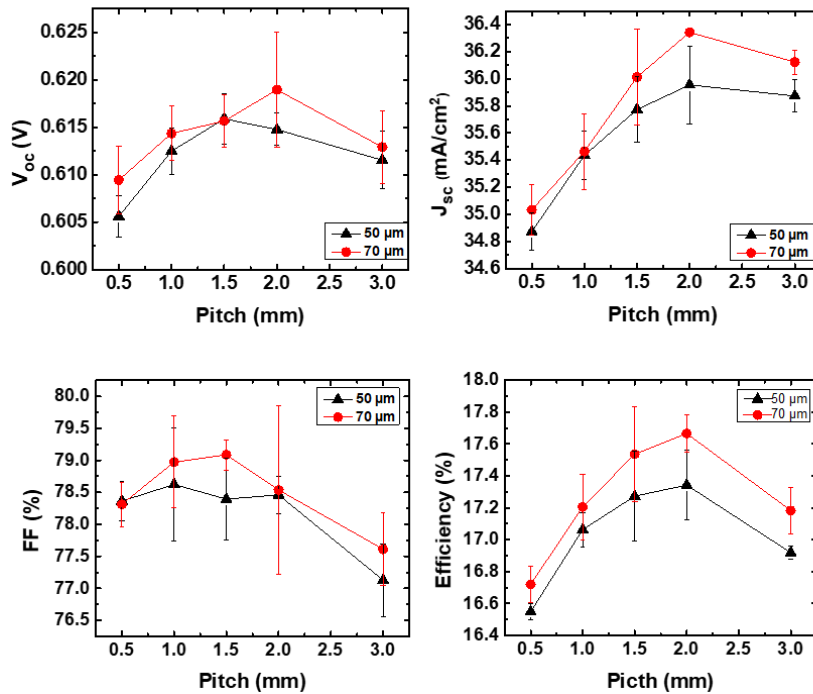


Figure 5.5. I-V results

Since small size solar cells (4 cm²) were produced from a full wafer, some of the results have big error margins due to inhomogeneous passivated wafers and local mechanical damages on the wafers formed during the processes (Figure 5.14). Based on the metallization fraction, it is expected that V_{oc} and I_{sc} increases and then tends to stay constant while FF decreases with pitch increment. Considering the error bars, we have a similar trend that is also compatible with the literature (Wolf et al., 2010; Zanuccoli et al., 2012).

V_{oc} decreases with the increased metalized area. However, when the V_{oc} graph is examined, it can be seen that the samples have higher V_{oc} when contact width is 70 μm compared to the 50 μm contact width case. Although the metalized area is bigger for the 70 μm , having higher BSF depth and less void presence compared to 50 μm case results in higher V_{oc} values. The void ratio and BSF depth values for both cases are shown in the following Table 5.1.

Table 5.1. *Contact Characteristics such as max Al:BSF depth and void percentage for 50 and 70 μm contact width cases*

Contact width (μm)	<i>Number of investigated contact</i>	<i>Max BSF depth(μm)</i>	<i>Void Percentage (%)</i>
50	17	2.5	70
70	12	5	20

The contact characteristics and their effects on the solar cell performance will be discussed in the further sections very explicitly. In the end, we decided to use 1 mm, 1.5 mm and 2 mm contact pitch for the next study.

5.3. Laser Ablation Properties

The ablated area on the stack of the passivation layer and SiN_x capping layer was investigated by SEM and the optical microscope, and an example image for both is given in Figure 5.6.

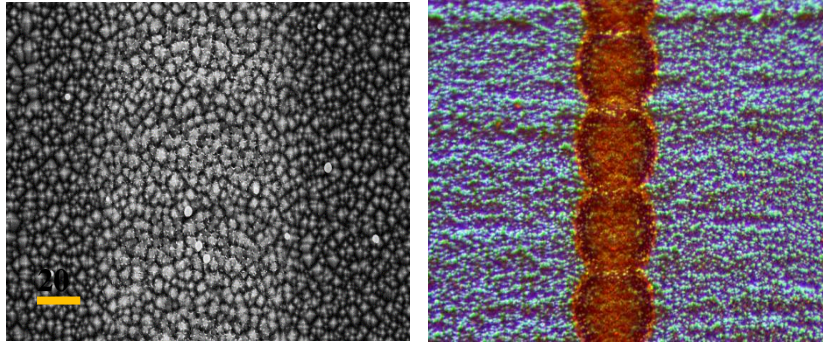


Figure 5.6. SEM image of an ablated area when 1.8 J/cm² fluence is used and optic image of an ablated area when 4.2 J/cm² fluence is used

At least 10 lines were inspected for each fluence and widths of the openings were measured. The relation between the width of the ablated area and fluence is represented in Figure 5.7. There is a linear relation between them. However, it is not perfectly linear due to the overlap of the pulses calculated according to Eqn 5.1 which causes a slight increase in the line width compared to single pulse ablation. For instance, the width was ~105 μm for %0 overlap and it was ~115 μm for %93 overlap when 200 kHz of frequency was used at max power (18.4 W). As power increases the effect of the overlap on the width also increases.

$$\text{Overlap ratio } (Q_f) = \left(1 - \frac{\text{Markspeed } (v)/\text{frequency } (f)}{\text{Beam Diameter } (D) + \text{markspeed } (v) * \text{pulse duration}(t)} \right) \quad (5.1)$$

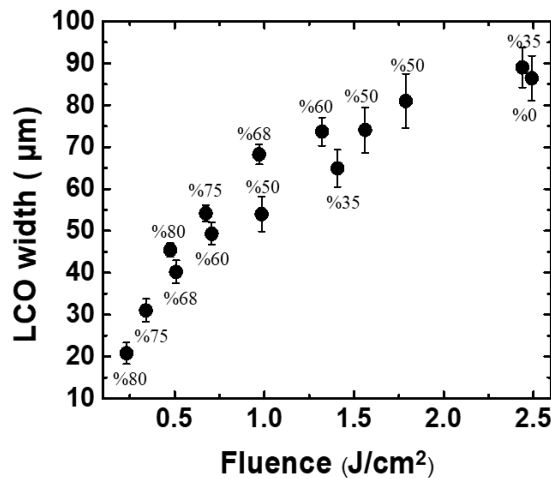


Figure 5.7. The relation between LCO width and fluence.

As another example, the width is larger for the 2.43 J/cm² fluence case where the overlap is %35 at 312 kHz (16.8 W) compared to 2.48 J/cm² fluence case where the overlap is %0 at 200 kHz (11 W power). Since our max scan speed is 20 m/s, single-pulse ablation can only be observed for 200 kHz among the applied frequencies. The overlap values for each fluence are given on the graph in Figure 5.7.

5.4. The Effects of the Laser Parameters on Contact Characteristics

In this section the effects of the laser parameters on contact characteristics such as BSF depth, contact width and void fraction were examined when the pitch was 1 mm, 1.5 mm and 2 mm. The BSF depth and the width of the rear contacts were measured from the SEM images and their correlation with the fluence of the picosecond laser was determined. Measured contact width was multiplied with $1/\sqrt{2}$ because the cleavage angle relative to the LCO lines was measured as 45° and the crack propagates along (100) direction which is over the diagonal of the wafers used. As mentioned in the Literature Survey part, the rear contacts can be categorized as follows: filled contact, void contact, partial void contact. An example SEM image for each category is shown in Figure 5.8, where also the contact width and BSF depth are indicated.

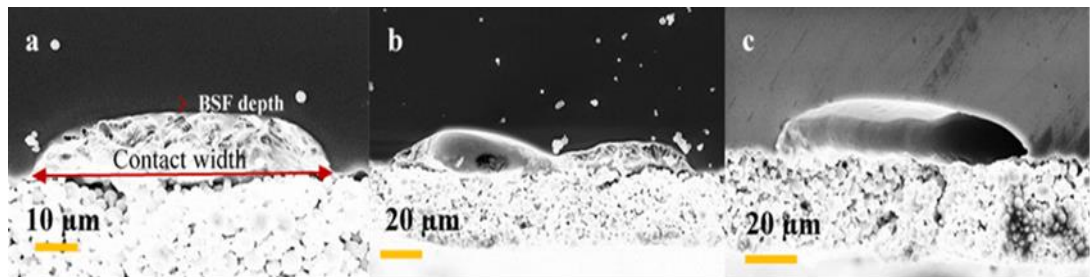


Figure 5.8. An example SEM image for filled contact (a) partial void contact (b) void contact (c).

The contact characteristics were independent of the pitch since the distance between LCOs is already bigger than the lateral diffusion of the Si in Al paste as shown in the EDAX result (Figure 5.9). More specifically, Si diffuses in Al melt until it saturates and hence bigger the distance between the LCOs the more unsaturated Al melt is available. However, the lateral propagation of Si in the Al matrix mainly depends on the peak firing temperature and it is ~ 500-600 μm in our case (Urrejola et al., 2011).

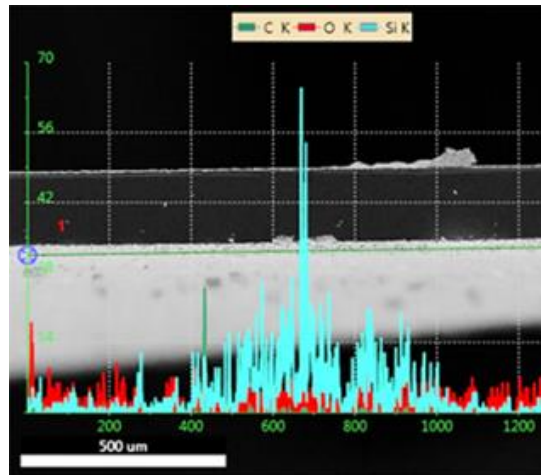


Figure 5.9. EDAX line analysis on the Al paste

For simplicity, one of the pitch cases, 1 mm due to the higher number of investigated contacts, was discussed. Max Al:BSF depth, average contact width values for each fluence are given in Table 5.2 where also calculated void and partial void fractions according to the investigated contacts are presented.

Table 5.2. Tabulated results of the experiment for 1 mm contact pitch case

Fluence (J/cm ²)	P_{avg} (W)	# of investigated contacts	Contact width (μm)	Max BSF depth (μm)	Void Fraction (%)	Partial Void Fraction (%)
0.23088	5.1	No contact	-	-	-	-
0.33953	6	26	34	2.5	85	4
0.47534	10.5	29	56	2.9	34	3
0.50703	7	27	53	3.8	48	33
0.6734	11.9	29	69	3	48	14
0.70622	7.8	13	57	3.2	54	31
0.9706	13.4	14	68	4.5	29	36
0.98464	8.7	27	74	4.2	26	52
1.32191	14.6	29	87	4.3	24	38
1.40746	9.7	24	86	4.1	17	46
1.56184	13.8	29	91	6.5	14	55
1.78819	15.8	30	100	6.1	10	30
2.43766	16.8	31	108	6	6	84
2.48989	11	29	89	5.5	24	38
4.16491	18.4	29	107	6.2	0	38

As can be seen in Figure 5.10, contact width (between 0,3-1,8 J/cm² fluence range) and Al:BSF depth (between 0,3-1,5 J/cm² fluence range) increases gradually and then increase slows down with a further laser fluence increment. Moreover, there is no contact formation for the 0.23 fluence case, which means the passivation layer was not completely removed. Hence the threshold fluence is between 0.23-0.33 J/cm².

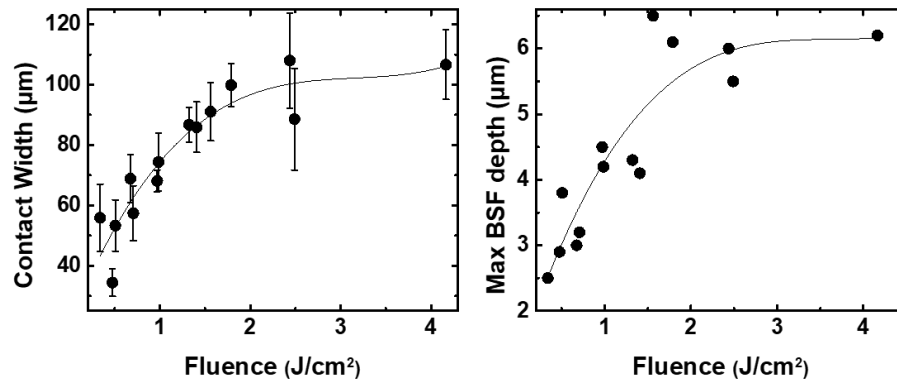


Figure 5.10. Contact width and max BSF depth values for each fluence. Lines are given for the visual aid

Also, void and partial void presence were examined for each fluence. The contact shapes shown in Figure 5.11 are counted as partial void. More specifically, contacts that have any eutectic presence are denoted as partial voids. Although there was no trend for the partial void fraction, the void presence was reduced with fluence increment which is related to LCO width. The relation of the void fraction with the fluence and LCO width is presented in Figure 5.12.

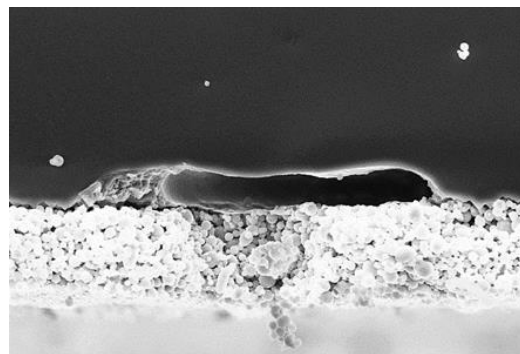


Figure 5.11. An example SEM image of a partial void

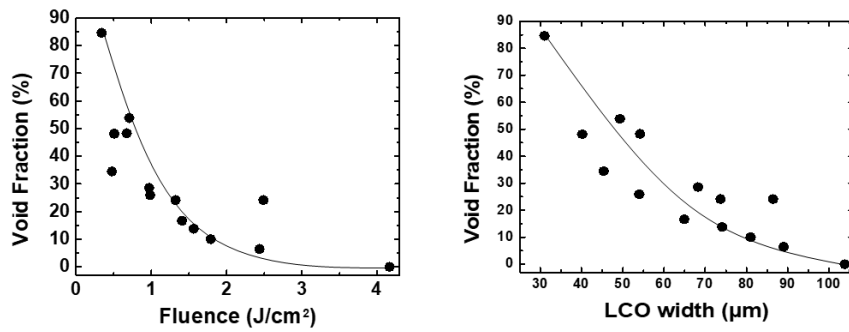


Figure 5.12. Void fraction relation with fluence and LCO width. The lines are given for the visual aid.

There are 2 explanations for the void formation process which are Kirkendall effect and surface energy minimization theory. These explanations are discussed in the section of “The Void Formation Mechanisms” in Chapter 3. As the contact width becomes narrow, less Si will be available for the dissolution in the liquid Al and void presence was seen when peak concentration of the Si in the paste above the LCO is insufficient (Lauermann, 2016). Indeed, the peak concentration below the eutectic concentration %12 results in voids with no BSFs. The profile of the Si concentration over the distance from LCO and time-dependent lateral movement in Al paste can be examined in the following Figure 5.13.

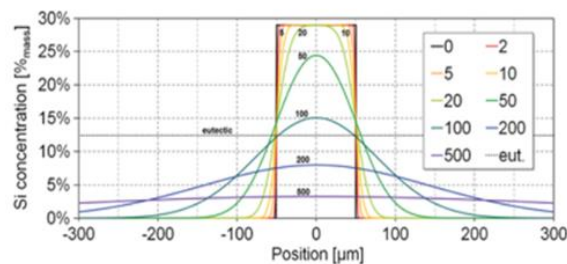


Figure 5.13. Si lateral distribution in the Al paste over the position to LCO according to time dependent spread (σ) that are presented with the color coding (Lauermann, 2016).

According to surface minimization theory, increment in the surface tension of the Al-Si melt prevents the adhesion of Al-Si melt to the Si bulk surface. According to the study (Kranz et al., 2016), a higher void presence is observed with deeper contacts. This was related to the increased surface area with contact depth. For our case, the

similar trend between void fraction and contact depth is observed. However, void fraction decreases with increased interface surface area calculated by the production of contact depth and contact width.

5.5. The Effects of Laser Parameters on Solar Cell Performance

In this part of the thesis work, the effects of the laser fluence and respectively contact behaviors on the solar cell performance were investigated through efficiency results. For this purpose, small size (2x2) solar cells were produced for each fluence given in Table 5.2 with 1mm, 1.5 mm and 2 mm pitch. The results are given in Fig 5.16, where the efficiency results belong to min 1 max 3 solar cells. Since 15 solar cells were produced from a wafer and 9 wafers were used in total, inhomogeneous passivation, mechanical damage on these wafers (Figure 5.14) and rare non-uniform front metallization (Figure 5.15) are some of the reasons of the error bars.

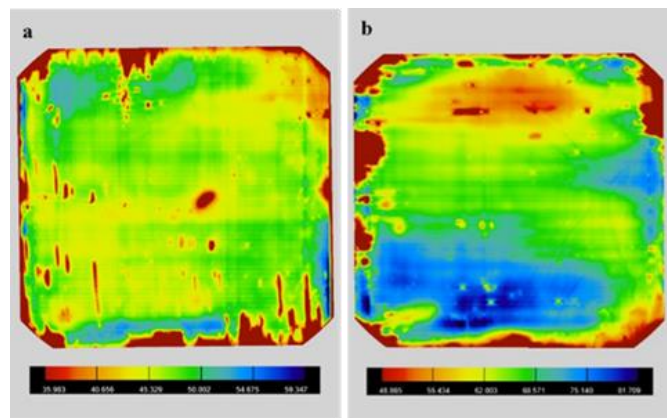


Figure 5.14. PL images that shows scratches (mechanical damage) on a wafer (a) and non-uniform passivation (b). Color bar shows the average life time values in terms of μs

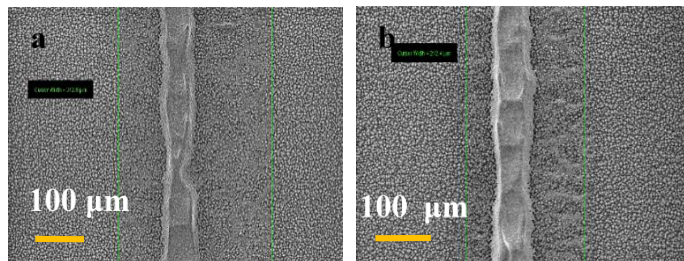


Figure 5.15. Front finger SEM images that indicates non-uniform spread of silver which are 312 μm (a) and 212 μm (b)

In the LCO approach by laser ablation, parameters such as rear contact width and pitch size, LCO geometry, local back surface field (BSF) depth, and void formation are some of the parameters that affect the cumulative recombination and series resistance of the cell thereby changing open-circuit voltage and FF. To decrease recombination, higher BSF depth and reduced rear contact fractions are needed. On the other hand, reduced void and partial void fraction, higher rear contact fraction should be provided to reduce series resistance losses. In agreement with this trade-off, an optimized range is determined as 0.5-1.8 J/cm² according to the efficiency results presented in Figure 5.16. It can be concluded that shallower BSF depth and higher void fraction leads to higher recombination and higher series resistance respectively between 0.3-0.5 J/cm² fluence range.

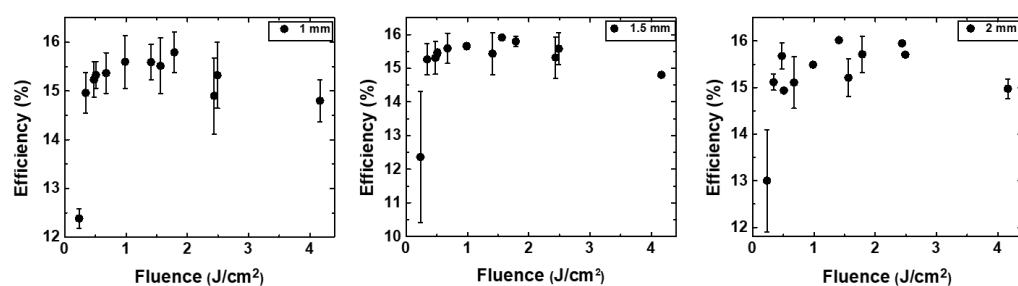


Figure 5.16. Efficiency results according to laser fluence when 1mm, 1.5 mm and 2 mm pitch is applied.

For more detail investigation, corresponding efficiencies were calculated for each fluence by 2D device simulation Quokka. For each fluence rear contact width, BSF depth and void fraction changes. However, we assumed that there is no void formation and changed the other parameters in the simulation. Recombination current at the metal-semiconductor interface (J_{0BSF} contacted) also changes with BSF depth and taken from (Rauer et al., 2011). The input parameters for the simulation are given in Table 5.3. and modified parameters are marked with red.

The Quokka simulated efficiency results when the pitch was 1 mm are shown in Figure 5.17. Since there were 3 solar cells for each fluence, 1 mm case is statistically more reliable. As it is seen on the graph in the Figure 5.17a, the slight difference of

metalized area between fluence case 1.8 J/cm² (contact width 100 μm) and 4.2 J/cm² (contact width 110 μm) did not affect the solar cell performance. Hence it is concluded that recombination current at the conductive boundaries is higher for 4.2 J/cm² fluence case, leading to higher cumulative recombination and lower efficiencies. One of the possible reasons for this situation could be lighter BSF doping which increases contact resistivity and sheet resistance as well as J_{0BSF}. According to the new estimated lighter BSF doping profile, J₀ was calculated from EDNA2 and contact resistivity value was taken from (Urrejola et al., 2010). Since the effect of the BSF sheet resistance on solar cell performance is too small, it is neglected. The corresponding efficiency of these new input parameters was calculated and given in Figure 5.17b.

Table 5.3. *Input parameters utilized for Quokka simulation*

Parameter	Value	Measurement Method
Cell Thickness	170 μm	SEM imaging
Front finger width	200 μm	SEM imaging
Front finger pitch	1600 μm	SEM imaging
Shading width	140 μm	From Literature
Front Contact resistivity	4 mΩcm ²	TLM
Emitter sheet resistance (R _{sheet})	71.2 Ω/□	ECV profiling
Junction depth	0.605 μm	ECV profiling
J ₀ emitter passivated	120 fA/cm ²	QSSPC
J ₀ emitter contacted	500 fA/cm ²	From literature
Bulk resistivity	1.4 Ω	QSSPC
Bulk lifetime τ _{bulk}	100 μs	QSSPC
Al:BSF Sheet Resistance (R _{sheet})	18 Ω/□	ECV profiling
Al:BSF depth	1-6 μm	SEM imaging
Rear contact width	35-110 μm	SEM imaging
Rear metal contact resistivity	3 mΩcm ²	From Literature
J _{0BSF} contacted	Changed according to BSF depth	From literature
J ₀ passivated rear	13.1f A/cm ²	From Literature
Shunt resistance ρ _{shunt}	150000 Ω cm ²	Suns-Voc

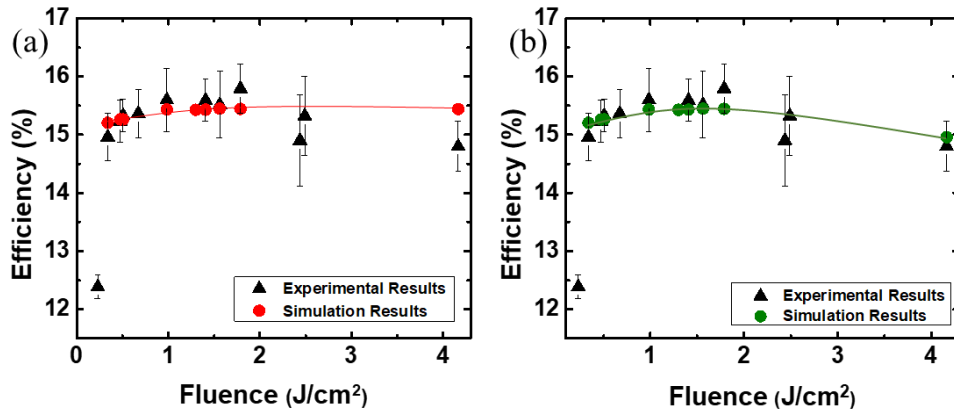


Figure 5.17. Calculated efficiency results with identical doping profile assumption (a) and when doping profile changed for fluence 4.2 J/cm² (b) for 1 mm pitch case.

The same trend can be observed when the pitch was 1.5 mm and 2 mm (Figure 5.18).

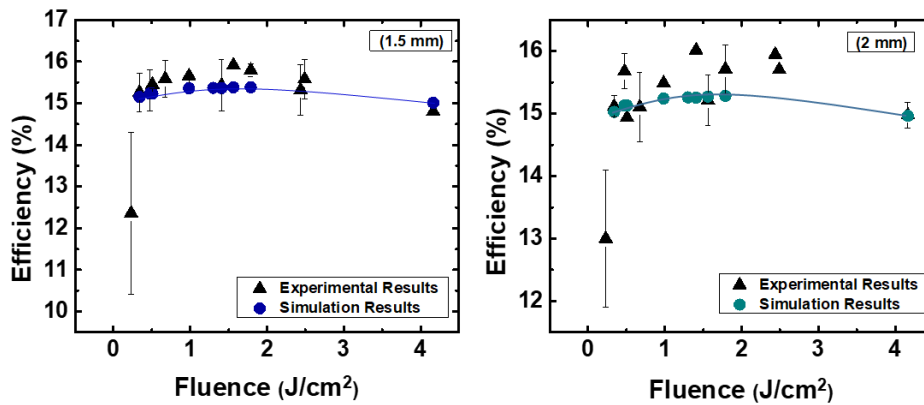


Figure 5.18. Calculated efficiency results when doping profile changed for fluence 4.2 J/cm² for 1.5 and 2 mm pitch cases

Another possible reason for the higher recombination at conductive boundaries could be laser-induced defects at high fluence. As can be seen in Figure 5.19 heat-affected zone is bigger for the fluence case 4.2 J/cm². This may lead to defects at the metal-semiconductor interface and hence higher recombination rate. Also, a minor contribution could come from BSF inhomogeneity at high fluence caused by surface morphology. It is reported that roughness of the surface increases BSF inhomogeneity and therefore J_{0BSF} , which leads to %0.08 efficiency difference between the polished and textured surface (Jianwen et al., 2014).

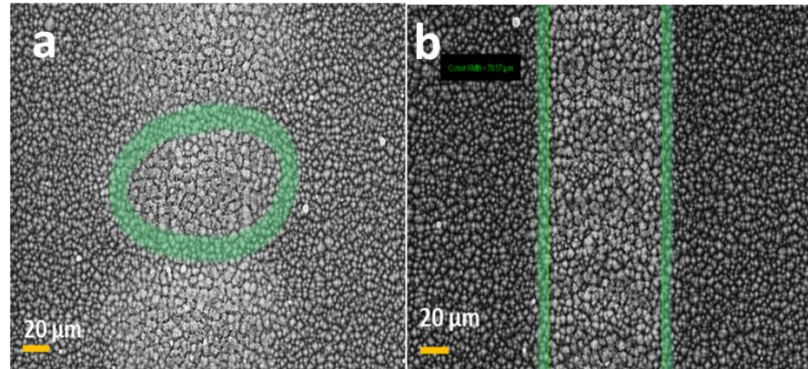


Figure 5.19. SEM images when fluence was 4.2 J/cm² (a) and 1.8 J/cm² (b). The heat-affected zone is highlighted in green.

To conclude, an optimized fluence range for laser processing was determined as 1-1.8 J/cm² according to simulated and experimental results.

Lastly, 60 solar cells with a size of 121 cm² were produced in Günam Photovoltaic Line (GPVL) by applying chosen fluence. The solar cell performance of the best cell is given in Table 5.4.

Table 5.4. Solar cell performance of the best sample

Type of Travel	V_{oc} (mV)	J_{sc} (mA/cm ²)	FF (%)	Efficiency (%)
Best Sample (110x110 mm)	648.7	38.8	75.7	19.04

CHAPTER 6

CONCLUSIONS

Solar photovoltaic technology is receiving more attention due to efficiency improvements with reduced fabrication cost and PERC type c-Si solar cell has one of the biggest market share of the industry due to its high performance/cost ratio. Although the first PERC structure was introduced in 1989, it took 25 years to improve low-cost processes for especially rear contacts and the rear passivation layer. Thanks to the technological improvements that are achieved, it is expected that PERC will be the dominant type of the market in a few years (ITRPV,2019). Hence, it is important to achieve higher efficiencies as possible and one way of doing that optimization of every process step.

The rear contact formation is affected by Al paste thickness and confined printing, Si content in Al paste, Al particle size in the paste, firing profile, metallization fraction, laser parameters. In this thesis work, the effects of the metallization fraction and laser parameters were investigated by keeping the others constant. In this way, the laser ablation process was optimized for PERC production.

Before starting the major experimental study, we conducted a series of experiments to determine a firing recipe as a controlled parameter. It is observed that Al:BSF gets deeper up to 12 μm with more time for interaction between liquid Al and solid Si which enables more dissolved Si in Al paste. However, efficiencies of solar cells with thicker BSFs were lower, which could be resulted from wider front silver widths. Considering the thermal budget and efficiency results we decided to use a profile similar to the standard firing profile used in the industry.

Ablated areas on the passivation layer investigated through a microscope, SEM. LCO width values were determined for each fluence and it is observed that LCO width

increases with fluence increment. Consequently, contact width increases gradually between 0,3-1,8 J/cm² fluence range and then increase slows down with a further increase in the laser fluence. LCO width value was 80 μm for 1.8 J/cm² case and 110 μm for 4.2 J/cm² case while contact width value was 100 μm for 1.8 J/cm² case and 110 μm for 4.2 J/cm². This leads to that 110 μm opening provides enough Si concentration to saturate Al melt at the solid Si - liquid Al interface. On the other hand, BSF depth increases gradually between 0,3-1,5 J/cm² fluence range and then increase slows down with a further increase in the laser fluence. Moreover, there was just one or two contact formation for the 0.23 fluence case, which means the passivation layer was not completely removed. Hence the threshold fluence is between 0.23-0.33 J/cm². Void fraction, which is explained by either Kirkendall effect and surface energy minimization theory, was reduced with fluence increment.

Cumulative recombination and series resistance are affected by parameters such as LCO geometry, back surface field (BSF) thickness and void formation, rear contact width and pitch size in terms of rear contact definition. Higher BSF depth, reduced rear contact width and void fraction are needed to reduce cumulative recombination. On the other hand, the lower series resistance is achieved by higher metallized areas, reduced void and partial void formation. To summarize, a minimized metallization area with higher BSF depth and minimized void formation are needed for higher efficiencies. In agreement with this, an optimized fluence range was investigated and determined as 1-1.8 J/cm². Between 0.3 and 0.5 J/cm² fluence, shallower BSF depth and higher void formation lead to a drop in efficiency. According to efficiency results calculated from Quakka, shallower BSF depth between 0.3 and 0.5 J/cm² fluence results in an approximately %0.2 efficiency drop. On the other hand, the effect of the metallized area difference between 1.8 and 4.2 J/cm² on the calculated efficiency results is approximately %0.02. However, the corresponding experimental efficiency results show that the efficiency for the 4.2 J/cm² fluence case much lower than the 1.8 J/cm² fluence case, which is related to higher recombination at the rear conductive boundaries. This could be caused by laser-induced defects at high fluence or doping

level of the BSF layer. Also, a minor contribution could come from BSF inhomogeneity resulted from increased surface roughness at high fluence.

Lastly, %19 solar cell efficiency has been achieved with industrial-scale solar cells produced in Günam Photovoltaic Line (GPVL). In this production, higher efficiencies were achieved compared to pitch study and laser fluence effect on solar cell performance study despite the larger solar cell area, which is directly related to front contact metallization. In this large scale production, narrower ($\sim 35\mu\text{m}$) and uniform silver front fingers were achieved.

REFERENCES

- Agostinelli, G., Delabie, A., Vitanov, P., & Alexieva, Z. (2006). Very low surface recombination velocities on p-type silicon wafers passivated with a dielectric with fixed negative charge, *90*, 3438–3443. <https://doi.org/10.1016/j.solmat.2006.04.014>
- Agostinelli, G., Szlufcick, J., Choulat, P., & Beaucarne, G. (2005). 20th European Photovoltaic Solar Energy Conference , 6-10 June 2005 , Barcelona , Spain 20th European Photovoltaic Solar Energy Conference , 6-10 June 2005 , Barcelona , Spain, (June), 942–945.
- Ali, Y., Shanmugam, V., Khanna, A., Wang, P., Balaji, N., Vigare, R., ... Mueller, T. (2019). Analysis of nanosecond and femtosecond laser ablation of rear dielectrics of silicon wafer solar cells. *Solar Energy Materials and Solar Cells*, *192*(December 2018), 117–122. <https://doi.org/10.1016/j.solmat.2018.12.002>
- Blakers, A. W., & Green, M. A. (1986). 20% Efficiency Silicon Solar Cells. *Applied Physics Letters*, *48*(3), 215–217. <https://doi.org/10.1063/1.96799>
- Byskov-Nielsen, J. (2010). Short-pulse laser ablation of metals : Fundamentals and applications for micro-mechanical interlocking. *Applied Physics*, (August), 96.
- Chen, Y., Altermatt, P. P., Dong, J., Zhang, S., Liu, J., Chen, D., ... Verlinden, P. J. (2014). Al-alloyed local contacts for industrial PERC cells by local printing. *2014 IEEE 40th Photovoltaic Specialist Conference, PVSC 2014*, (June), 3322–3325. <https://doi.org/10.1109/PVSC.2014.6925645>
- Cornagliotti, E., Tous, L., & Russell, R. (2012). Integration of Inline Single-side Wet Emitter Etch in PERC Cell Manufacturing Energy Procedia Integration of inline single-side wet emitter etch in PERC cell manufacturing, (December). <https://doi.org/10.1016/j.egypro.2012.07.120>
- Dressler, K., Kratt, M., Voss, P. A., Ebert, S., Herguth, A., & Hahn, G. (2016). Influence of Al Particle Size and Firing Profile on Void Formation in Rear Local Contacts of Silicon Solar Cells, *6*, 68–73.
- Dullweber, T., & Schmidt, J. (2016). Industrial Silicon Solar Cells Applying the Passivated Emitter and Rear Cell (PERC) Concept-A Review. *IEEE Journal of Photovoltaics*, *6*(5), 1366–1381. <https://doi.org/10.1109/JPHOTOV.2016.2571627>
- Gatz, S., Müller, J., Dullweber, T., & Brendel, R. (2012). Analysis and optimization of the bulk and rear recombination of screen-printed PERC solar cells. *Energy Procedia*, *27*, 95–102. <https://doi.org/10.1016/j.egypro.2012.07.035>

- Gatz, Sebastian, Hannebauer, H., Hesse, R., Werner, F., Schmidt, A., Dullweber, T., ... Brendel, R. (2011). screen-printed silicon solar cells pss, *149*(4), 147–149. <https://doi.org/10.1002/pssr.201105045>
- Gautero, L., Hofmann, M., Rentsch, J., Bitnar, B., Sallese, J., & Preu, R. (2009). All-screen-printed 120- μ M-thin large-area silicon solar cells applying dielectric rear passivation and laser-fired contacts reaching 18 % efficiency, (May 2014). <https://doi.org/10.1109/PVSC.2009.5411562>
- Green, M. A. (2015). The Passivated Emitter and Rear Cell (PERC): From conception to mass production. *Solar Energy Materials and Solar Cells*, *143*, 190–197. <https://doi.org/10.1016/j.solmat.2015.06.055>
- Hofmann, M., Kania, D., Rentsch, J., Preu, R., Saint-Cast, P., & Benick, J. (2009). Very low surface recombination velocity on p-type c-Si by high-rate plasma-deposited aluminum oxide. *Applied Physics Letters*, *95*(15), 151502. <https://doi.org/10.1063/1.3250157>
- ITRPV. International Technology Roadmap for Photovoltaic. no. September, page 42, 2019
- Jianwen, D., Concord, G., Limited, H., Weiwei, D., Chen, D., Solar, T., ... Solar, T. (2014). Effect of Rear Surface Morphology on Al-Bsf Uniformity of Silicon Solar Cells. *29th European Photovoltaic Solar Energy Conference and Exhibition*, (c), 1059–1061.
- Kim, J., Hwang, Y., Kim, J., Lim, J., & Lee, E. (2014). Investigation of rear side selective laser ablation and damage etching process for industrial PERC solar cells. *Energy Procedia*, *55*, 791–796. <https://doi.org/10.1016/j.egypro.2014.08.061>
- Kim, M., Park, S., & Kim, D. (2013). Highly efficient PERC cells fabricated using the low cost laser ablation process. *Solar Energy Materials and Solar Cells*, *117*, 126–131. <https://doi.org/10.1016/j.solmat.2013.04.025>
- Kranz, C., Baumann, U., Wolpensinger, B., Lottspeich, F., Müller, M., Palinginis, P., ... Dullweber, T. (2016). Void formation in screen-printed local aluminum contacts modeled by surface energy minimization. *Solar Energy Materials and Solar Cells*, *158*, 11–18. <https://doi.org/10.1016/j.solmat.2016.06.039>
- Kray, D., Hermle, M., & Glunz, S. W. (2008). Theory and Experiments on the Back Side Reflectance of Silicon Wafer Solar Cells, (May 2007), 1–15. <https://doi.org/10.1002/pip>
- Lacey, S. (2018, August 23). By 2023, the World Will Have 1 Trillion Watts of Installed Solar PV Capacity. Retrieved from <https://www.greentechmedia.com/articles/read/by-2023-the-world-will-have-one-trillion-watts-of-installed-solar-pv-capaci#gs.9Y8SIT0>

- Lauermann, T. (2016). The influence of contact geometry and sub-contact passivation on the performance of screen printed AL₂O₃ passivated ..., (November). <https://doi.org/10.4229/26thEUPVSEC2011-2DO.1.6>
- Lauermann, T., Fröhlich, B., Hahn, G., & Terheiden, B. (2015). Diffusion-based model of local Al back surface field formation for industrial passivated emitter and rear cell solar cells. *Progress in Photovoltaics: Research and Applications*, 23(1), 10–18. <https://doi.org/10.1002/pip.2388>
- Merchant, E. (2018, January 16). IRENA: Global Renewable Energy Prices Will Be Competitive With Fossil Fuels by 2020. Retrieved from <https://www.greentechmedia.com/articles/read/irena-renewable-energy-competitive-fossil-fuels-2020#gs.Qdxjcs8>
- Müller, J., Bothe, K., Gatz, S., & Brendel, R. (2012). Modeling the formation of local highly aluminum-doped silicon regions by rapid thermal annealing of screen-printed aluminum. *Physica Status Solidi - Rapid Research Letters*, 6(3), 111–113. <https://doi.org/10.1002/pssr.201105611>
- Müller, J., Müller, J., Bothe, K., Gatz, S., Plagwitz, H., Schubert, G., & Brendel, R. (2011). Contact Formation and Recombination at Screen-Printed Local Aluminum-Alloyed Silicon Solar Cell Base Contacts, (November 2016). <https://doi.org/10.1109/TED.2011.2161089>
- Münzer, K. A., Hein, M., Schöne, J., Hanke, M., Teppe, A., & Schlosser, R. E. (2012). Technical performance and industrial implementation in favour of centaurus technology, 27, 631–637. <https://doi.org/10.1016/j.egypro.2012.07.121>
- Preu, R., & Lu, R. (2002). Laser-Fired Rear Contacts for Crystalline Silicon Solar Cells, 34(October 2001), 29–34. <https://doi.org/10.1002/pip.422>
- Rauer, M., Schmiga, C., Krause, J., Woehl, R., Hermle, M., & Glunz, S. W. (2011). Further analysis of aluminum alloying for the formation of p+ regions in silicon solar cells. *Energy Procedia*, 8(February 2014), 200–206. <https://doi.org/10.1016/j.egypro.2011.06.124>
- Schmidt, J., Kerr, M., & Cuevas, A. (2001). Surface passivation of silicon solar cells using plasma-enhanced chemical-vapour-deposited SiN films and thin thermal SiO₂/plasma SiN stacks. *Semiconductor Science and Technology*, 16(3), 164–170. <https://doi.org/10.1088/0268-1242/16/3/308>
- Smets, A. H., Jäger, K., van Swaaij, R. A., & Zeman, M. (2016). Losses and Efficiency Limits. *Solar Energy: The Physics and Engineering of Photovoltaic Conversion, Technologies, and Systems*, 127–135. Retrieved from https://ocw.tudelft.nl/wp-content/uploads/solar_energy_section_10_1_10_2.pdf
- Stockum, W., & Rohatgi, A. (2006). INVESTIGATION OF MODIFIED SCREEN-PRINTING AL PASTES FOR LOCAL BACK SURFACE FIELD

FORMATION, *1*, 1338–1341.

- Urrejola, E., Peter, K., Plagwitz, H., & Schubert, G. (2010). Al-Si alloy formation in narrow p-type Si contact areas for rear passivated solar cells. *Journal of Applied Physics*, *107*(12). <https://doi.org/10.1063/1.3437070>
- Urrejola, E., Peter, K., Plagwitz, H., & Schubert, G. (2011). Silicon diffusion in aluminum for rear passivated solar cells. *Applied Physics Letters*, *98*(15). <https://doi.org/10.1063/1.3579541>
- Veith, B., Werner, F., Zielke, D., Brendel, R., & Schmidt, J. (2011). Comparison of the thermal stability of single Al₂O₃ layers and Al₂O₃/SiN_x stacks for the surface passivation of silicon. *Energy Procedia*, *8*(April), 307–312. <https://doi.org/10.1016/j.egypro.2011.06.141>
- Vladoiu, I., Stafe, M., Negutu, C., & Popescu, I. M. (2009). Influence of the pulse number and fluence of a nanosecond laser on the ablation rate of metals, semiconductors and dielectrics. *The European Physical Journal Applied Physics*, *47*(3), 30702. <https://doi.org/10.1051/epjap/2009100>
- Werner, F., Stals, W., Görtzen, R., Veith, B., & Brendel, R. (2011). High-rate atomic layer deposition of Al₂O₃ for the surface passivation of Si solar cells. *Energy Procedia*, *8*(April), 301–306. <https://doi.org/10.1016/j.egypro.2011.06.140>
- Wolf, A., Biro, D., Nekarda, J., Stumpp, S., Kimmerle, A., MacK, S., & Preu, R. (2010). Comprehensive analytical model for locally contacted rear surface passivated solar cells. *Journal of Applied Physics*, *108*(12). <https://doi.org/10.1063/1.3506706>
- Yacob Ali, J. M., Shanmugam, V., Lim, B., Aberle, A. G., & Mueller, T. (2018). Femtosecond laser ablation of dielectric layers for high-efficiency silicon wafer solar cells. *Solar Energy*, *164*(October 2017), 287–291. <https://doi.org/10.1016/j.solener.2018.02.046>
- Zanuccoli, M., De Rose, R., Magnone, P., Sangiorgi, E., & Fiegna, C. (2012). Performance analysis of rear point contact solar cells by three-dimensional numerical simulation. *IEEE Transactions on Electron Devices*, *59*(5), 1311–1319. <https://doi.org/10.1109/TED.2012.2187297>
- Zhao, J., Wang, A., Abbaspour-Sani, E., Yun, F., & Green, M. A. (1997). Improved efficiency silicon solar cell module. *IEEE Electron Device Letters*, *18*(2), 48–50. <https://doi.org/10.1109/55.553040>
- Zimmermann, G., Barkenfelt, B., Suva, K., Wendt, J., Kaden, T., Rupp, S., ... Thalheim, O. T. (n.d.). No Title, 821–826.
- World Energy Outlook 2018. Retrieved from <https://www.iea.org/weo2018/>

APPENDIX

A. Publication

Es, F., Semiz, E., Orhan, E., Genç, E., Kökbudak, G., Baytemir, G., & Turan, R. (2019). Optimization of PERC fabrication based on loss analysis in an industrially relevant environment: First results from GÜNAM photovoltaic line (GPVL). *Renewable Energy*